

Identification of sources of potential fields with the continuous wavelet transform: Two-dimensional wavelets and multipolar approximations

Pascal Sailhac

Laboratoire de Proche Surface, Ecole et Observatoire des Sciences de la Terre-Institut de Physique du Globe de Strasbourg, Centre National de la Recherche Scientifique and Université Louis Pasteur, Strasbourg, France

Dominique Gibert

Géosciences Rennes, Centre National de la Recherche Scientifique and Université Rennes 1, Rennes, France

Received 11 June 2002; revised 5 December 2002; accepted 31 January 2003; published 20 May 2003.

[1] We show new continuous wavelet-based transformation techniques of potential field maps and propose interpretation schemes for characterizing three-dimensional (3-D) sources having some finite extent. As in previous studies, we use wavelets derived from the Poisson kernel which generate a position-altitude representation of potential field data initially measured at one level above the ground. We use first-order or second-order wavelets to obtain wavelet transform parameters related to the 3-D analytic signals or 3×3 tensors of the data. We show how such parameters can be used to characterize the sources, first, by using the assumption of their local homogeneity and, second, by using multipolar expansions to estimate the sizes of the horizontal or vertical extent of the 3-D source. Thus we generalize to 3-D the Taylor expansion of upward continued 2-D analytic signals previously shown for the interpretation of profiles transformed using complex wavelets. Such a 3-D interpretation scheme based upon position-altitude representations has been developed to interpret the maps of scalar potential field anomalies (e.g., magnetic total field anomalies or vertical gravity anomalies) but can be also used for upward continued maps of vector or tensor of potential field anomalies as obtained by new surveys of the full tensor of gravity; this also concerns the interpretation of derived potentials considered in poroelasticity and electrokinetic in porous materials of the Earth. We illustrate the technique on synthetic data; in addition, a first application on aeromagnetic data from French Guyana shows the potential of the technique. **INDEX TERMS:** 0903 Exploration Geophysics: Computational methods, potential fields; 0920 Exploration Geophysics: Gravity methods; 0925 Exploration Geophysics: Magnetic and electrical methods; 3260 Mathematical Geophysics: Inverse theory; 3299 Mathematical Geophysics: General or miscellaneous; **KEYWORDS:** wavelets, magnetics, harmonic/multipolar expansion, upward continuation, analytic signals, Guyane Française

Citation: Sailhac, P., and D. Gibert, Identification of sources of potential fields with the continuous wavelet transform: Two-dimensional wavelets and multipolar approximations, *J. Geophys. Res.*, 108(B5), 2262, doi:10.1029/2002JB002021, 2003.

1. Introduction

[2] The high-resolution achieved for the most recent magnetic, gravity and electric self-potential surveys stimulates the development of specific interpretation techniques which emphasize the information of interest to both geologists and geophysicists. In addition to classical measurements of the vertical gravity anomalies or the magnetic total field anomalies, this concerns also the interpretation of three-component gradients and 3×3 -component tensor surveys [Bell et al., 1997; Biegert and Millegan, 1998;

Grauch and Millegan, 1998] or electric gradients of self-potential surveys [Gibert and Pessel, 2001; Sailhac and Marquis, 2001].

[3] The purpose of the interpreter is the recovery of the causative sources of potential fields data acquired above the ground. One approach is the inversion in which one numerically compares observed data to synthetic data resulting from models of the underground sources. It is well known that this is both mathematically and numerically ill posed and practical solutions can be obtained only when reliable a priori constraints can be added to the problem [Tarantola and Valette, 1982; Blakely, 1996]. Another approach is the processing for which observed data are transformed into other fields (Fourier transform,

upward continuation, derivatives, reduction to the pole) where the desired information is hopefully enhanced [Gibert and Galdeano, 1985]. Furthermore, these transformed fields can then be used to improve inversion procedures: for example, using derivatives in the Fourier domain [Pilkington, 1997] or using upward continuation [Fedi and Rapolla, 1999].

[4] We have explored the use of wavelet transforms, as initially introduced in the analysis of potential fields by Moreau [1995]. The principle of this method is to compare data with Green's functions resulting from multipolar sources at various depths and positions underground. In practice, this consists in interpreting potential fields data via the properties of the upward continued and differentiated field. Moreau *et al.* [1997] have demonstrated the general n -dimensional theory for local homogeneous sources. Moreau *et al.* [1999] have analyzed the effects of noise and extent of sources on the properties of the wavelet coefficients. Sailhac *et al.* [2000] have used one-dimensional complex wavelet coefficients similar to upward continued analytic signals. They demonstrated, in the case of total field magnetic anomaly profiles, some useful relations between parameters of the wavelet coefficients and the apparent inclination of magnetization, in addition to depth, vertical extent, and dip angle of the sources. Martelet *et al.* [2001] have applied similar relations to the case of gravity profiles.

[5] We now present specific properties of two-dimensional wavelet coefficients. To demonstrate their properties, we use their relations to quantities classically considered in potential field interpretation techniques, namely: the modulus of the 3-D analytic signal [Nabighian, 1984; Roest *et al.*, 1992] and the norm of the potential field tensor [Pedersen and Rasmussen, 1990]. Essential properties follow from upward continuation operator which gives a position-altitude representation of these quantities in a way similar to that of Hornby *et al.* [1999], who used 2-D wavelet coefficients defined by horizontal derivatives and upward continuation of potential field maps [Le Mouél, 1970; Bhattacharyya, 1972; Baranov, 1975].

[6] First, we present definitions and recall the general inversion scheme for local homogeneous sources. This is illustrated in the case of a point, line and strip gravity sources. Second, we develop multipole approximations in case of extended sources, and we show application to synthetic potential fields caused by triaxial ellipsoids and rectangular prisms of finite size. The theory is also illustrated to part of a large aeromagnetic data of French Guyana previously analyzed on the basis of profiles [Sailhac *et al.*, 2000]. This last illustration is kept short for the aim of conciseness of the paper; this shows how to characterize depth extension of a sedimentary lens by interpreting scaling behavior of 2-D wavelet transform coefficients.

2. Basic Theory

2.1. General Definitions

[7] First, we recall the definitions of the basic theory and write them for the 2-D case considered in this paper [Moreau *et al.*, 1997, 1999]. The relevant parameters are listed in the notation section. We define the continuous

wavelet transform of a function $\phi_0(\mathbf{h})$ of the horizontal position vector $\mathbf{h} = (x, y)^t$ as a convolution product,

$$\mathcal{W}_{\psi|\phi_0}(\mathbf{b}, a) = \int_{R^2} \psi\left(\frac{\mathbf{b} - \mathbf{h}}{a}\right) \phi_0(\mathbf{h}) \frac{d^2h}{a^2} = (\mathcal{D}_a \psi * \phi_0)(\mathbf{b}), \quad (1)$$

where $\mathbf{b} = (b_x, b_y)^t$ is a translation vector, $a \in R^+$ is a dilation parameter, and the dilation operator \mathcal{D}_a acts on the analyzing wavelet $\psi(\mathbf{h})$ as

$$\mathcal{D}_a \psi(\mathbf{h}) = \frac{1}{a^2} \psi\left(\frac{\mathbf{h}}{a}\right). \quad (2)$$

[8] We use a special class of analyzing wavelets defined by applying an homogeneous Fourier multiplier of degree $\gamma \geq 1$ (basically equivalent to a derivative of order γ) to the Poisson semigroup kernel [Moreau *et al.*, 1997, 1999]:

$$P_a(\mathbf{h}) = \frac{1}{2\pi} \frac{a}{(a^2 + |\mathbf{h}|^2)^{3/2}}. \quad (3)$$

The operator $\langle P_a(\mathbf{h}) * |$ defines the well-known upward continuation of harmonic fields $\phi(\mathbf{h}, z)$ from measurement level z to level $z + a$ [Le Mouél, 1970; Bhattacharyya, 1972; Galdeano, 1974; Baranov, 1975; Gibert and Galdeano, 1985]. The basic homogeneous Fourier multiplier of interest is the oblique fractional derivative of order γ which, in the 3-D physical space, acts as

$$\mathcal{O}_q^\gamma \equiv \nabla^\gamma \cdot \mathbf{q}, \quad (4)$$

where $\nabla^\gamma = (\partial^\gamma/\partial x^\gamma, \partial^\gamma/\partial y^\gamma, \partial^\gamma/\partial z^\gamma)^t$ defines the generalized gradient operator and \mathbf{q} is a 3-D unit vector defining the direction of the oblique derivative. It must be emphasized that although acting on the three directions of the physical space, the coupling between \mathbf{h} and the vertical direction z implied by the Poisson equation enables this operator to be applied through a convolution restricted to the 2-D variable \mathbf{h} . All classical transformation operators, like the reduction to the pole, used to process potential field data may be obtained by successively applying the \mathcal{O} operator with, possibly, a negative γ [e.g., Gibert and Galdeano, 1985]. Accordingly, analyzing wavelets are generated through

$$\psi_{\mathbf{Q}}^\gamma(\mathbf{h}) = \langle \mathcal{O}_{\mathbf{q}_1}^{\gamma_1} * \mathcal{O}_{\mathbf{q}_2}^{\gamma_2} * \dots * \mathcal{O}_{\mathbf{q}_N}^{\gamma_N} * P_1(\cdot) \rangle(\mathbf{h}), \quad (5)$$

where $\gamma = \sum \gamma_i$ and \mathbf{Q} is a matrix whose N columns are the \mathbf{q}_i vectors. A wavelet belonging to this class is, for instance (Figure 1),

$$\psi_{\mathbf{x}}^1(x, y) = \frac{3}{2\pi} \frac{-x}{(x^2 + y^2 + 1)^{5/2}}, \quad (6)$$

$$\psi_{\mathbf{x}}^2(x, y) = \frac{3}{2\pi} \frac{(4x^2 - y^2 - 1)}{(x^2 + y^2 + 1)^{7/2}}. \quad (7)$$

Vertical wavelets $\psi_{\mathbf{z}}^1$ may as well be defined.

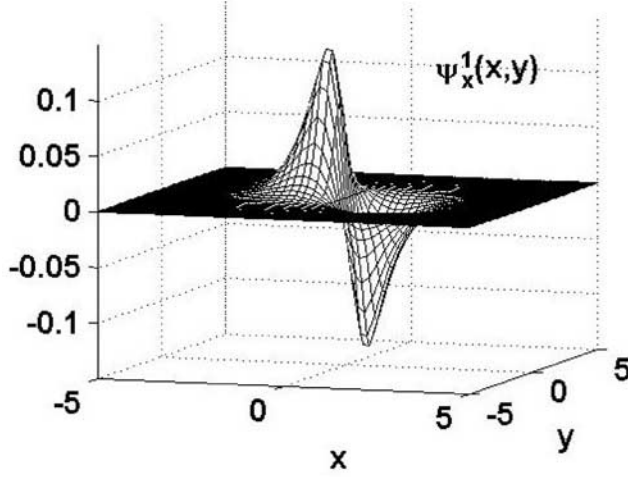


Figure 1. Example of a 3-D wavelet belonging to the Poisson semigroup class and defined as $\psi_{\mathbf{x}}^1(\mathbf{h}) = \mathcal{O}_{\mathbf{x}}^1 * P_1(\mathbf{h})$ (see equation (6)).

[9] In the general case, the wavelet transform may be expressed either as a tensorial or vectorial quantity whose L components are obtained by successively convolving different analyzing wavelets with the observed field $\phi_0(\mathbf{h})$. Among these most general vectorial wavelets Ψ , the ones whose components have the same total order of derivative γ are particularly interesting since all components share a common physical dimension (e.g., nT/m²) and may then be subsequently combined to derive relevant quantities like angles and modulus. In the remaining of this paper, we shall call $\Psi_{\mathbf{T}}^{\gamma}$ such a wavelet with a total derivative order γ related to some vectorial or tensorial combination of derivatives labeled \mathbf{T} . The most general tensorial wavelet transform is then given by

$$\mathcal{W}_{\Psi_{\mathbf{T}}^{\gamma}|\phi_0}(\mathbf{b}, a) = (\mathcal{D}_a \Psi_{\mathbf{T}}^{\gamma} * \phi_0)(\mathbf{b}). \quad (8)$$

The components of the wavelet transform are simply the upward continued maps of the oblique derivatives of the initial data ϕ_0 .

[10] An example of vectorial wavelet is the horizontal gradient

$$\Psi_{\mathbf{G}}^1(\mathbf{h}) = \underbrace{\begin{pmatrix} \mathcal{O}_{\mathbf{x}}^1 \\ \mathcal{O}_{\mathbf{y}}^1 \end{pmatrix}}_{\mathbf{G}} * P_1(\mathbf{h}), \quad (9)$$

and a tensorial wavelet is, for instance, the tensor of the horizontal second-order derivatives

$$\Psi_{\mathbf{H}}^2(\mathbf{h}) = \underbrace{\begin{pmatrix} \mathcal{O}_{\mathbf{x}}^2 & \mathcal{O}_{\mathbf{x}}^1 * \mathcal{O}_{\mathbf{y}}^1 \\ \mathcal{O}_{\mathbf{x}}^1 * \mathcal{O}_{\mathbf{y}}^1 & \mathcal{O}_{\mathbf{y}}^2 \end{pmatrix}}_{\mathbf{H}} * P_1(\mathbf{h}). \quad (10)$$

2.2. Relations With Classical Quantities

[11] Definition (8) allows recovery of all classical quantities computed from geophysical potential fields. For

instance, the real and imaginary parts of the 3-D analytic signal $A_1(\mathbf{h})$ [Roest *et al.*, 1992] correspond to the components of the following vectorial analyzing wavelet:

$$\Psi_{A_1}^1(\mathbf{h}) = \underbrace{\begin{pmatrix} \mathcal{O}_{\mathbf{x}}^1 + \mathcal{O}_{\mathbf{y}}^1 \\ \mathcal{O}_{\mathbf{z}}^1 \end{pmatrix}}_{\mathbf{A}_1} * P_1(\mathbf{h}), \quad (11)$$

where we recall that the derivative in the z direction is actually obtained through a convolution over the \mathbf{h} variable. Using this wavelet, the upward continued analytic signal is given by

$$A_1(\mathbf{b}, z + a) = \frac{1}{a} (1, i) \cdot \mathcal{W}_{\Psi_{A_1}^1|\phi_0}(\mathbf{b}, a). \quad (12)$$

In the same way, the γ -order analytic wavelet coefficients corresponding to the generalized 3-D analytic signal $A_{\gamma} \equiv (\partial^{\gamma-1}/\partial z^{\gamma-1})A_1$ of Hsu *et al.* [1998] may be obtained with the analyzing wavelet given by:

$$\Psi_{A_{\gamma}}^{\gamma}(\mathbf{h}) = \underbrace{\begin{pmatrix} \mathcal{O}_{\mathbf{x}}^1 * \mathcal{O}_{\mathbf{z}}^{\gamma-1} + \mathcal{O}_{\mathbf{y}}^1 * \mathcal{O}_{\mathbf{z}}^{\gamma-1} \\ \mathcal{O}_{\mathbf{z}}^{\gamma} \end{pmatrix}}_{\mathbf{A}_{\gamma}} * P_1(\mathbf{h}). \quad (13)$$

The modulus of these 3-D analytic signals are given by the Euclidean norm of the corresponding vectorial wavelet transforms. For elongated 2-D structures like dikes and faults, equation (11) simplifies into

$$\Psi_{A_1}^1(\mathbf{h}) = \begin{pmatrix} \mathcal{O}_{\mathbf{p}}^1 \end{pmatrix} * P_1(\mathbf{h}), \quad (14)$$

where the \mathbf{p} vector is the direction perpendicular to the strike of the structure. In such a case, both components of the vectorial wavelet transform are Hilbert transforms of each other, and the norm of the wavelet transform is the envelope of each component with its maximum located above the 2-D features (e.g. dikes and faults). In magnetics, this property holds even without reduction to the pole since this latter operation corresponds either to a rotation of the analytic signal in the complex plane or to a rotation applied to the vectorial wavelet transform. Hence we observe that all operations classically performed onto the analytic signal may equivalently be done in the wavelet framework with the further advantage to allow for a scale-dependent analysis.

[12] Let us now turn to second-order tensorial wavelets related to the classical tensor of potential fields [Nelson, 1988; Pedersen and Rasmussen, 1990; Dransfield, 1994]. The fundamental 3×3 tensorial wavelet of interest is given by

$$\Psi_{\mathbf{S}}^2(\mathbf{h}) = \underbrace{\begin{pmatrix} \mathcal{O}_{\mathbf{x}}^2 & \mathcal{O}_{\mathbf{x}}^1 * \mathcal{O}_{\mathbf{y}}^1 & \mathcal{O}_{\mathbf{x}}^1 * \mathcal{O}_{\mathbf{z}}^1 \\ \mathcal{O}_{\mathbf{x}}^1 * \mathcal{O}_{\mathbf{y}}^1 & \mathcal{O}_{\mathbf{y}}^2 & \mathcal{O}_{\mathbf{y}}^1 * \mathcal{O}_{\mathbf{z}}^1 \\ \mathcal{O}_{\mathbf{x}}^1 * \mathcal{O}_{\mathbf{z}}^1 & \mathcal{O}_{\mathbf{y}}^1 * \mathcal{O}_{\mathbf{z}}^1 & \mathcal{O}_{\mathbf{z}}^2 \end{pmatrix}}_{\mathbf{S}} * P_1(\mathbf{h}). \quad (15)$$

The tensorial wavelet transform of $\phi_0(\mathbf{h})$ is the normalized (factor a^2) upward continued tensor of ϕ_0 . In the remaining

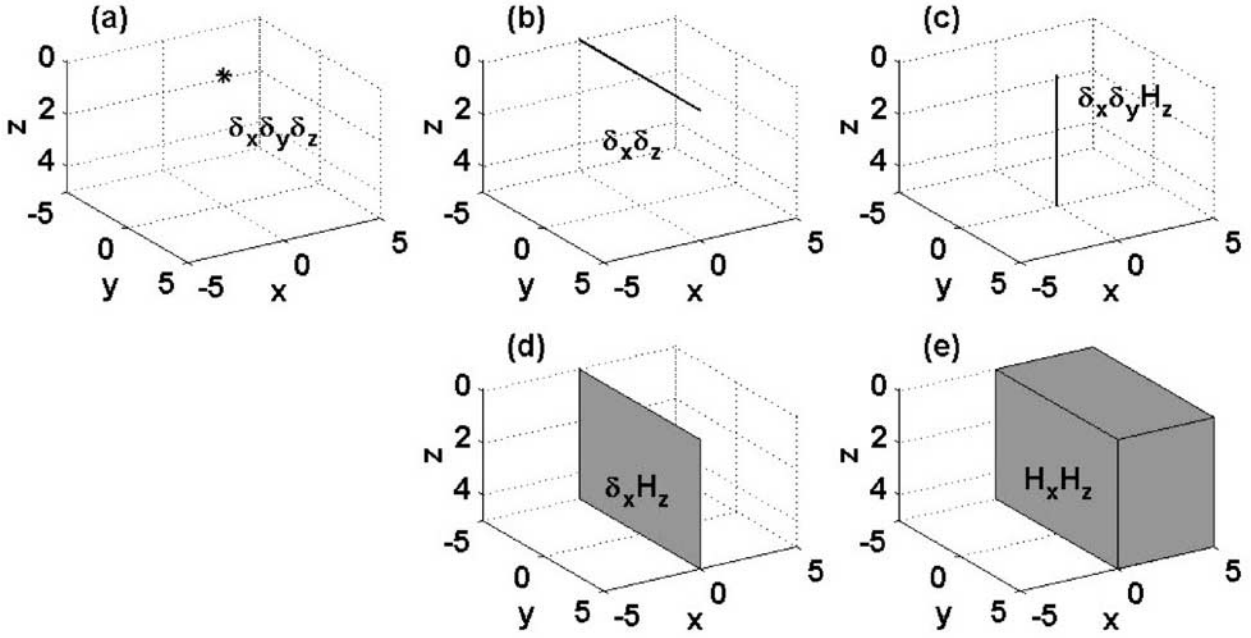


Figure 2. Examples of homogeneous functions at $x = y = z = 0$ with degree $\alpha \in -N$: (a) a point ($\delta_x \delta_y \delta_z$ has $\alpha = -3$), (b) a horizontal infinite line in y direction ($\delta_x \delta_z$ has $\alpha = -2$), (c) a vertical semi-infinite line in z ($\delta_x \delta_y H_z$ has $\alpha = -2$), (d) a vertical strip infinite in y and semi-infinite in z ($\delta_x H_z$ has $\alpha = -1$), and (e) a vertical contact infinite in y and semi-infinite in x and z ($H_x H_z$ has $\alpha = 0$). (Notation: $\delta_x = \delta(x)$ is the Dirac delta function at $x = 0$; $H_x = H(x)$ is the Heaviside step function equal to 1 for $x \geq 0$, 0 else.)

of this paper, the modulus of a tensorial wavelet is defined as being the Euclidean norm (sometimes referred to as the L_2 norm or the Frobenius norm) equals to the square root of the sum of the squared components.

2.3. Properties for Local Homogeneous Sources

[13] The class of wavelets defined in equation (5) gives remarkable properties to the wavelet transforms of potential fields produced by homogeneous sources [Moreau *et al.*, 1997, 1999]. Let us recall that the source function $\sigma(\mathbf{r})$ is homogeneous with degree α at $\mathbf{r} = (0, 0, 0)^T$ if, for any positive number λ , we have $\sigma(\lambda \mathbf{r}) = \lambda^\alpha \sigma(\mathbf{r})$. Such a source is characterized both by its depth z_0 and its homogeneity degree α which is a shape parameter. Simple instances (see Figure 2) are the point source ($\alpha = -3$, σ is a 3-D Dirac function), the horizontal line source with infinite extent ($\alpha = -2$, σ is a 2-D Dirac function), the vertical strip source with infinite extent ($\alpha = -1$, σ is the product of a 1-D Dirac function and a 1-D Heaviside step function), and the vertical contact source with infinite extent ($\alpha = 0$, σ is the product of two 1-D Heaviside step functions).

[14] Moreau *et al.* [1997, 1999] have shown that the wavelets obtained through equation (5) make the wavelet transform sharing the homogeneity properties of the homogeneous source causing the analyzed potential field. These relations give a generalization of those reported thirty years ago for the decrease of the upward continued tensor components with altitudes [Hammer, 1971]. This translates by a coupling between the horizontal position

vector \mathbf{b} and the dilation a under the form of an homogeneity relationship:

$$\mathcal{W}_{\Psi_T^\gamma|\phi_0}(\mathbf{b}, a) = (a/a')^\gamma \lambda^\beta \mathcal{W}_{\Psi_T^\gamma|\phi_0}(\lambda \mathbf{b}, a'), \quad (16)$$

where $\lambda = (a' + z_0)/(a + z_0)$ involves the source depth z_0 , and β is an exponent depending on both the homogeneity degree α of the source and the physical nature of potential field ϕ_0 . Indeed, $\beta = \alpha - \gamma$ for the magnetic field, $\beta = \alpha - \gamma + 1$ for gravity, and $\beta = \alpha - \gamma + 2$ for the Newtonian potential. The homogeneity property of equation (16) indicates that the entire wavelet transform may be extrapolated from its values taken on an arbitrary plane $a = \text{constant}$. This geometrically translates into the fact that the wavelet transform has a cone-like appearance defined by a set of lines such that $(b_x, b_y)/(z_0 + a) = (1, 1) \times \text{const}$. The apex of the cone is located at the source place.

2.4. Wavelet Modulus Maxima Interpretation

[15] Like in profile analysis [Moreau *et al.*, 1999; Sailhac *et al.*, 2000; Martelet *et al.*, 2001], let us now consider the modulus maxima of wavelet coefficients (also called ridges or skeleton). They are determined using classical procedures of local maxima detection and have the useful property of being located nearby above the sources and having good signal to noise ratios. Modulus maxima are classically used in edge detection of images, and Hornby *et al.* [1999] have already shown images of the 3-D skeleton resulting from potential field maps, that focus to the edges of potential field sources. They use a horizontal analyzing

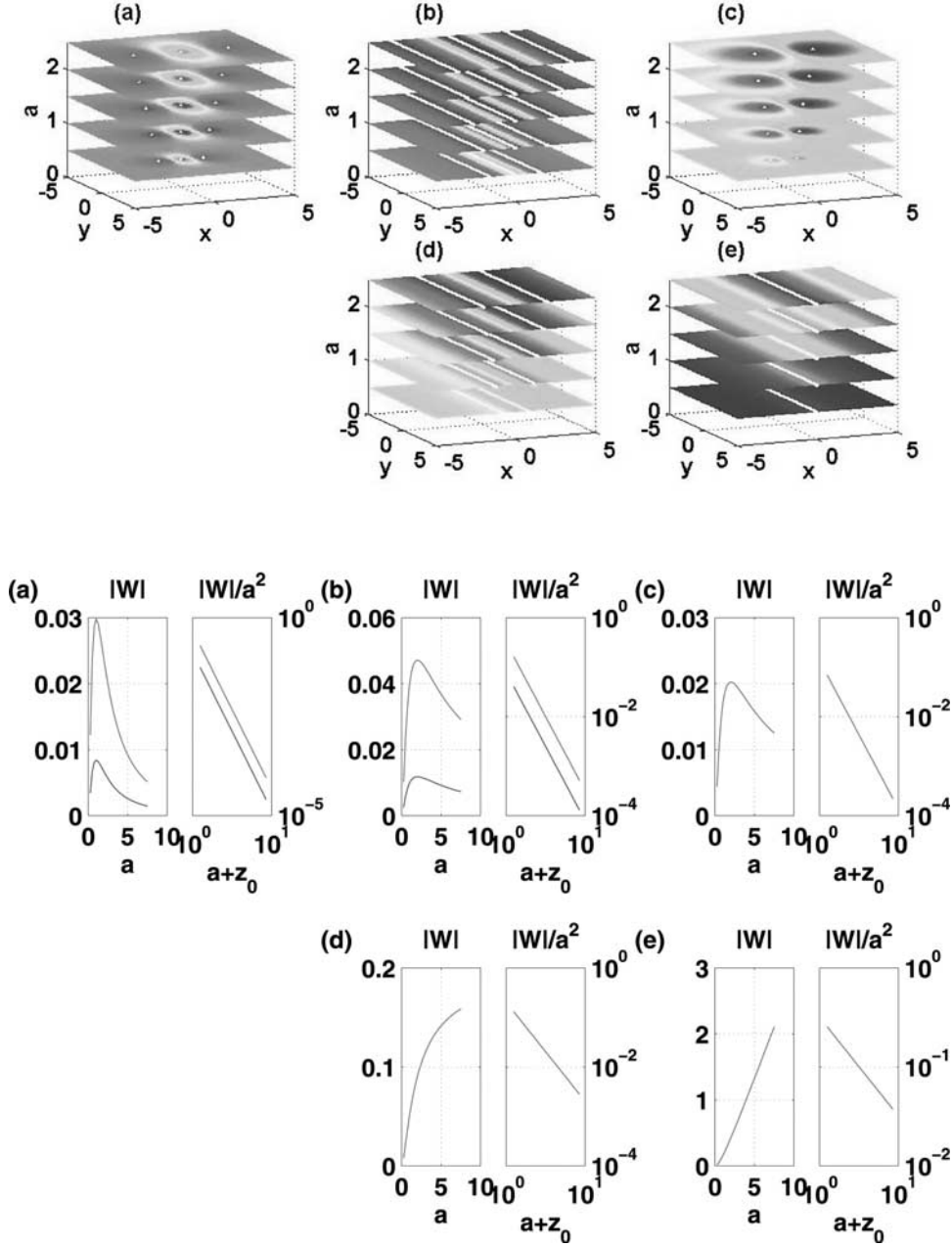


Figure 3. Typical scaling relations of the potential field wavelet modulus maxima for local homogeneous sources following to functions shown in Figure 2 and translated to the depth $z = z_0$ (Figures 3a–3e correspond to Figures 2a–2e). We show both the 3-D skeleton (top in white) and the log-log plots of the normalized amplitudes $|\mathcal{W}_a|/a^\gamma$ versus translated altitudes $a + z_0$ (bottom). In this figure, we only consider the case of vertical gravity fields analyzed with the second-order $\psi_x^2(\mathbf{h})$ wavelet defined in equation (7) and cone-like structures appear in xz sections. See color version of this figure at back of this issue.

wavelet equal to the first component of the vectorial wavelet defined in equation (11). Equation (16) provides interpretation possibilities of the modulus of the wavelet coefficients.

[16] A first step in the interpretation of the wavelet transform is to search for the top of cone-like structures from 3-D skeleton of the modulus maxima. This yields location of homogeneous local sources without any prior idea about their homogeneity degree α (Figure 3). How-

ever, such a 3-D geometrical procedure needs sophisticated graphical implementations to be useful in a computer-aided interpretation program. As shown in previous papers [Moreau *et al.*, 1999; Sailhac *et al.*, 2000; Martelet *et al.*, 2001], we instead prefer to invert equation (16) along each line defined in the modulus maxima by using a series of linear regressions in log-log plots, and by testing for a range of trial depths z_0 . In practice, this is done by plotting $\log(|\mathcal{W}_a|/a^\gamma)$ versus $\log(a + z_0)$ and by searching the z_0

value which, according to equation (16), makes the relationship linear. Once the depth z_0 is obtained, the slope of the straight line directly gives the exponent β related to the homogeneity degree α . Thus both the depth z_0 and the shape parameter α of the source are estimated in a common procedure.

2.5. Comparison With Euler Deconvolution

[17] As previously observed by *Sailhac et al.* [2000], the homogeneity degree α of the source relates to the structural index N used in Euler deconvolution. This latter method is based upon the analysis of the homogeneity properties of the field ϕ_0 [Thompson, 1982; Reid et al., 1990; Huang, 1996; Ravat and Taylor, 1998]. However, N generally depends on some prior information introduced in the Euler deconvolution method. Conversely, the homogeneity degree α of the source is determined from the scaling exponent β alone computed from the wavelet transform without any prior information. Indeed, even the implicit assumption concerning the homogeneous nature of the sources may be checked by verifying the quality of the linear relationship presented above.

[18] *Sailhac et al.* [2000] give both β for 1-D wavelet transforms and $-N$ as a function of the homogeneity degree α of the source in different situations. These relations are still valid when β and $-N$ are obtained from 2-D wavelet transforms and magnetic potential maps ϕ_0 respectively. For instance, this means that a simple pole has $\alpha = -3$ while an infinite horizontal dike has $\alpha = -2$; the corresponding gravity fields g_z have $N = 2$ for the pole and $N = 1$ for the dike; and gravity field wavelet coefficients of order γ have $\beta = -\gamma - 2$ for the pole and $\beta = -\gamma - 1$ for the dike (in this formula, every γ derivation for the wavelets is perpendicular to the dike direction).

[19] Thus both Euler and wavelet techniques are designed to approach the inverse problem by characterizing potential field sources by simple combinations of local singularities. However, whereas Euler deconvolution benefited from recent improvements [Silva et al., 2001; Nabighian and Hansen, 2001], we prefer the wavelet domain approach for three main advantages: (1) it allows the estimation of both depths z_0 and homogeneity degrees α in a simple manner; (2) it includes an upward continuation procedure which provides useful symmetries between the wavelet transform domain and buried sources below, and also reduces high-frequency noise present in the data which may produce strong artefacts in Euler deconvolution; and (3) as will be shown in section 3, the wavelet approach simplifies the characterization of sources of finite extent.

3. Approximation in Multipolar Series

3.1. Question of Extended Sources

[20] The search for local homogeneous sources corresponds in applications, to the characterization of small bodies (with $\alpha \approx -3$) and to the border of semi-infinite bodies (with $\alpha \approx -2$ or $\alpha \approx -1$). However, the case of sources having a finite size is obviously the most common real case that we address now.

[21] A first approach is to analyze the wavelet transform in distinct dilation ranges (or altitudes) where it behaves

as for homogeneous sources. This may be possible provided the extended source has a sufficiently simple geometry. Consider, for example, a prismatic body with finite rectangular horizontal cross section, with a semi-infinite height, and with a top at relatively shallow depth (Figure 4). At very large dilations (i.e., large altitudes) the source body asymptotically appears as a vertical semi-infinite thin rod with $\alpha \approx -2$; conversely, in the small-dilation range, the sides of the prism produce independent cone-like structures in the wavelet transform with $\alpha \approx -1$, characteristic of vertical strip sources. If the height of the shallow prism is comparable to its horizontal extent, its large-dilation appearance is the one of a point source $\alpha \approx -3$, while the borders give $\alpha \approx -2$. This approach supposes that the extended source may be decomposed into a small number of elements behaving as homogeneous sources which may be separately analyzed. However, additional multipolar contributions around these regions of single homogeneity may blur the interpretation and prevent determination of α .

[22] A second and more realistic approach is then to consider the whole multipolar series approximation and to characterize the source extent via the misfit of the single homogeneity model of source. This has been done for profiles of *Sailhac et al.*, [2000] who give analytical expressions for typical 2-D bodies and exact power laws as in equation (16) for local sources at depth z_0 . The wavelet coefficients above a homogeneous source at depth z_0 scale as $(a + z_0)^{-\beta}$ where we recall that β depends both on the homogeneity α of the source and on the order γ of the wavelet. For extended sources, Taylor series may be calculated to analyze the discrepancy from this simple scaling due to the finite size of the body. The wavelet coefficients then involve an additional term of higher degree, $S \times (a + z_0)^{-(\beta+2)}$, where S is a factor depending on the shape and size of the source, but not on its depth.

3.2. From Grant and West to Wavelets

[23] Multipolar series approximations for extended sources are well known in potential field theory, but just a few attempted to apply it in interpretation. Let us recall the pioneering work of *Grant and West* [1965] which we apply to the wavelet coefficients by upward continuation and derivatives.

[24] Let us consider a Newtonian potential V at $\mathbf{r} = (x, y, z)^t$ out of the volume \mathcal{V} which contains the causative extended source of density ρ :

$$V(\mathbf{r}) = - \int_{\mathcal{V}} \frac{\rho(\mathbf{r}') d^3 r'}{|\mathbf{r} - \mathbf{r}'|}, \quad (17)$$

where the gravitational constant G has been omitted for simplicity of further equations. The multipole series expansion of V reads, in spherical coordinates (r, θ, ϕ) associated to position vector \mathbf{r} :

$$V(r, \theta, \phi) = - \sum_{l=0}^{\infty} \sum_{m=-l}^{m=l} \frac{B_l^m Y_l^m(\theta, \phi)}{r^{l+1}}, \quad (18)$$

where $Y_l^m(\theta, \phi) = \cos(m\phi) P_l^{|m|}(\cos \theta)$ are spherical harmonics defined from associated Legendre functions of

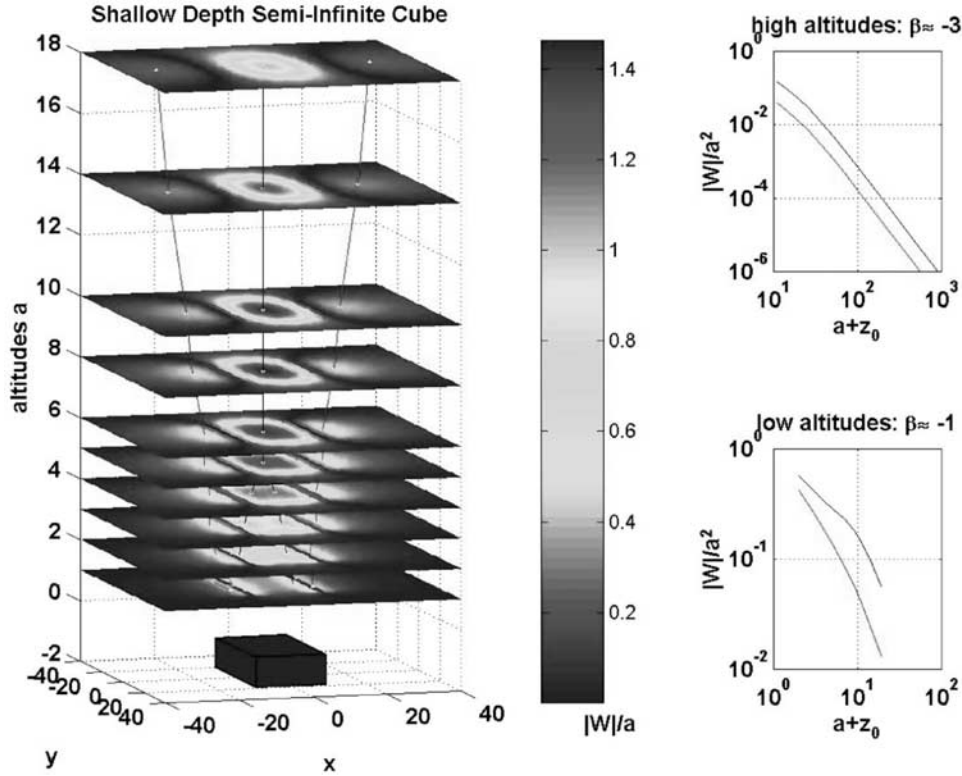


Figure 4. Different regions of potential field wavelet domain of extended sources: The gravity case of a rectangular prism of finite horizontal sizes $\Delta_1 = \Delta_2 = 10$ and semi-infinite height which top is relatively shallow, at $z_0 = 1$ (bottom left). Because of the source size, wavelet modulus maxima of the 3-D skeleton (left) exhibit different homogeneity behaviors depending on the region of focus (right): either at large altitudes (top right: $\beta \approx -3$, $\alpha \approx -2$), or at lower altitudes near to the border (bottom right: $\beta \approx -1$, $\alpha \approx 0$). We have used the wavelet $\psi_x^2(\mathbf{h})$ as in Figure 3. See color version of this figure at back of this issue.

degree l and order m , and B_l^m are coefficients depending only on the source distribution:

$$B_l^m = \frac{(l-m)!}{(l+m)!} \frac{\int_V \rho(r, \theta, \phi) r^l Y_l^m(\theta, \phi) dV}{\int_V \rho(r, \theta, \phi) dV}. \quad (19)$$

The first terms of the series (monopole in $1/r$ and dipoles in $1/r^2$) are enough to give a good approximation of the

potential field V for large r relative to the barycenter of the extended source. The corresponding first B_l^m coefficients can give a good idea of the sizes of the body source. For instance, *Grant and West* [1965] considered a triaxial ellipsoid, an elliptical cylinder and a rectangular bloc of constant density ρ and dimensions Δ_x , Δ_y , and Δ_z along x , y and z axis, respectively (see Figure 5 and Table 1). They proposed to estimate parameters B_0^0 , B_2^0 and B_2^2 by fitting a model on individual anomalies extracted from a survey.

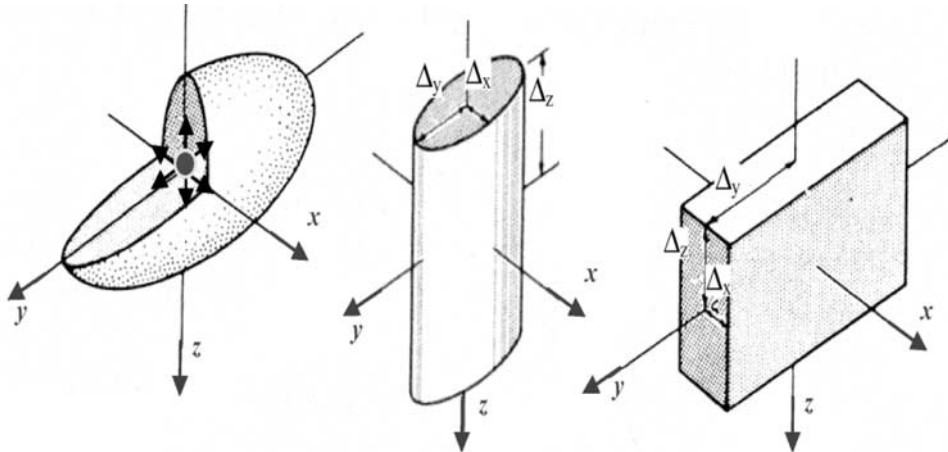


Figure 5. Examples of simple multipolar sources: Triaxial ellipsoid, cylinder, and rectangular prism. See color version of this figure at back of this issue.

Table 1. Principal Multipolar Parameters for the Three Source Examples Shown in Figure 5^a

Source Parameters	B_0^0	B_2^0/B_0^0	B_2^2/B_0^0
Triaxial ellipsoid	$4\pi\Delta_1\Delta_2\Delta_3$	$\frac{2\Delta_3^2 - \Delta_1^2 - \Delta_2^2}{10}$	$\frac{\Delta_1^2 - \Delta_2^2}{20}$
Elliptical cylinder	3	$\frac{8\Delta_3^2 - 3\Delta_1^2 - 3\Delta_2^2}{24}$	$\frac{\Delta_1^2 - \Delta_2^2}{16}$
Rectangular prism	$8\pi\Delta_1\Delta_2\Delta_3$	$\frac{2\Delta_3^2 - \Delta_1^2 - \Delta_2^2}{6}$	$\frac{\Delta_1^2 - \Delta_2^2}{12}$

^aFrom *Grant and West* [1965].

Such an extraction is generally difficult to perform because of the coalescence of the analyzed anomaly with nearby anomalies produced by other sources. This is why these multipolar expansions have not really been used in practice. This task becomes easier using the wavelet transform modulus maxima.

[25] By successive derivatives, one obtains gradient, tensor, and higher degrees of the potential (see, e.g., *Paul* [1961] for higher degrees of equation (17), and *Dransfield* [1994] for higher degrees of equation (18)). This gives the zeroth and first-order expansions of 2-D wavelet coefficients which may be used in the interpretation as shown for 1-D complex wavelet coefficients by *Sailhac et al.* [2000]. Wavelet coefficients $\mathcal{W}_{\psi^\gamma}(a)$ of order γ at modulus maxima above a source of parameters B_0^0 , B_2^0 and B_2^2 , can be approximated for large altitude a , by

$$|\mathcal{W}_{\psi^\gamma}(a)| \approx Ka^\gamma(z_0 + a)^\beta \left[B_0^0 + \frac{C_0 B_2^0 + C_2 B_2^2}{(z_0 + a)^2} \right], \quad (20)$$

where z_0 is the depth to the barycenter, β is related to the source homogeneity, K is an intensity factor, and both C_0 and C_2 are factors depending on the type of potential field analyzed and the direction of derivation used in the wavelets (see next sections).

[26] Zeroth-order corresponds to a local homogeneous source as seen for the point source in section 2.3 with $\alpha = -3$ (this applies similarly to other local homogeneous source having other homogeneity degree, like an infinite rod with $\alpha = -2$). So, for a Newtonian potential, the theoretical $\beta = -\gamma - 1$. This constraint can be used to estimate the barycenter depth z_0 from linear regressions in the log-log plots:

$$\ln \frac{|\mathcal{W}_{\psi^\gamma}(a)|}{a^\gamma} \approx \ln(KB_0^0) + \beta \ln(z_0 + a), \quad (21)$$

where the term $\ln(KB_0^0)$ is essentially a source related intensity factor. Residuals of the best linear regression can be used to characterize the first-order source parameters B_2^0 and B_2^2 .

[27] For instance, for a step-like source and using the magnetic field (for which $\beta = \alpha - \gamma$) along a profile, we introduced the following function $H(a)$ which converges rapidly to the height Δ_z of the step [*Sailhac et al.*, 2000]:

$$H(a) = 2(z_0 + a) \left| \ln \frac{|\mathcal{W}_{\psi^\gamma}(a)|}{a^\gamma} - \ln(KB_0^0) - \beta \ln(z_0 + a) \right|^{\frac{1}{\gamma}}. \quad (22)$$

This converges to $2\sqrt{|C_0 B_2^0 + C_2 B_2^2|/B_0^0}$. By using simultaneously wavelets in different directions, one obtains different combinations of B_0^0 , B_2^0 and B_2^2 which can be used for their individual estimations. In order to facilitate these estimations, we prefer to use the square size function $S_2(a)$ instead of $H = 2\sqrt{|S_2|}$:

$$S_2(a) = (z_0 + a)^2 \left[\ln \frac{|\mathcal{W}_{\psi^\gamma}(a)|}{a^\gamma} - k - \beta \ln(z_0 + a) \right], \quad (23)$$

which converges to $(C_0 B_2^0 + C_2 B_2^2)/B_0^0$ whatever the signs of involved parameters.

3.3. Wavelet Coefficients of Hornby et al.

[28] Let us first illustrate the multipolar series from equation (20) in case of the wavelet transform, $\mathcal{W}_{\psi_G^1|g_z}(\mathbf{b}, a)$, of the vertical component of the gravity field, $g_z(\mathbf{h}, z) = -\partial V(\mathbf{h}, z)/\partial z$, measured at level $z = 0$ as introduced by *Hornby et al.* [1999]:

$$\mathcal{W}_{\psi_G^1|g_z}(\mathbf{b}, a) = |\mathcal{W}_{\Psi_G^1|g_z}(\mathbf{b}, a)| \quad (24)$$

$$\mathcal{W}_{\psi_G^1|g_z}(\mathbf{b}, a) = a\sqrt{V_{xz}^2 + V_{yz}^2}, \quad (25)$$

where Ψ_G^1 is the horizontal gradient analyzing wavelet given in equation (9). The quantities V_{xz} and V_{yz} are the elements of the gravity tensor, $V_{ij}(\mathbf{h}, a)$, upward continued to the altitude a (see Appendix B) and corresponding to the x and y derivatives of $-g_z$ [*Hornby et al.*, 1999].

[29] In case of a spherical source at depth z_0 , and for which $B_2^0 = B_2^2 = 0$, *Hornby et al.* [1999] show that the maxima lines of $\mathcal{W}_{\psi_G^1|g_z}(\mathbf{b}, a)$ are located on concentric circles of radius $(z_0 + a)/2$ with an amplitude $48B_0^0 a(z_0 + a)^{-3}/25\sqrt{5}$, where $B_0^0 = GM$ (G is the gravitational constant and M is the mass of the source). As shown in Appendix C, equation (18) may be used to obtain the series expansion of sources elongated in the x , y and z directions. In this case, the parameters B_2^0 and B_2^2 are nonnull quantities (see Table 1), and the wavelet maxima make a cone-like structure corresponding to a revolution surface with Cassini oval cross sections (see Figure 6). Thus the maxima depend on the azimuthal angle of φ cylindrical coordinates with vertical axis passing through the barycenter, and follow

$$\mathcal{W}_{\psi_G^1|g_z}(\varphi, a) \approx \frac{48B_0^0 a}{25\sqrt{5}z_a^3} \cdot \left[1 + \frac{13\gamma_0 - 6\gamma_2 \cos 2\varphi}{25z_a^2} \right], \quad (26)$$

where $z_a^2 = (z_0 + a)^2$ with $z_a^2 \gg \gamma_0 = 10B_2^0/B_0^0$ and $z_a^2 \gg \gamma_2 = 10B_2^2/B_0^0$.

[30] Similarly, S_2 (equation (23)) depends on Δ when $B_2^2 \neq 0$. Because $\cos 2\varphi$ has zero mean over $[0, 2\pi)$, its azimuthal mean $\langle S_2 \rangle_\varphi(a)$ is a function of a only and converges to $C_0 B_2^0/B_0^0$ where $C_0 = 26/5$. By symmetries of $\cos 2\varphi$ maximum and minimum values of S_2 over $[0, 2\pi)$ converge to $(C_0 B_2^0 \pm C_2 B_2^2)/B_0^0$, where $C_2 = 12/5$; their difference $\Delta S_2|_{\max}(a)$ converge to $\pm 2C_2 B_2^2/B_0^0$ (and the maxima of S_2 over $[0, 2\pi)$ shows the direction of the main horizontal axis). These limits are new parameters to characterize the source geometry. For instance, by using Table 1 and assuming a triaxial ellipsoid source, the difference $\Delta S_2|_{\max}(a)$ informs about horizontal eccentricity (limit of $\frac{14}{5}|B_2^2/B_0^0| = \frac{7}{50}|\Delta_x^2 - \Delta_y^2|$) and the mean $\langle S_2 \rangle_\varphi(a)$ informs

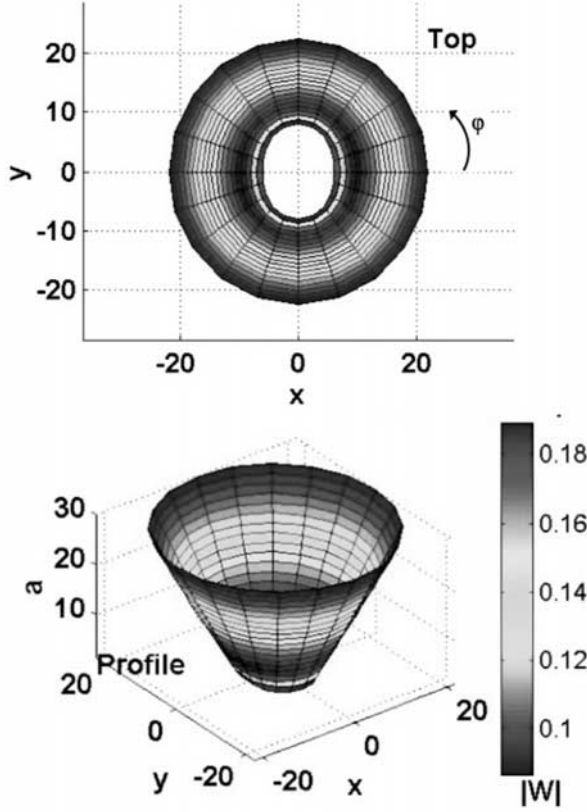
WTMM for a Triaxial ellipsoid with ($\Delta_x=3, \Delta_y=10, \Delta_z=10, z_0=15$)

Figure 6. Wavelet transform modulus maxima (WTMM) for a triaxial ellipsoid with semiaxis values $\Delta_x = 3$, $\Delta_y = \Delta_z = 10$, and $z_0 = 15$ ($B_0^0 = \frac{4}{3}\pi\Delta_x\Delta_y\Delta_z = 400\pi$, $B_2^0/B_0^0 = 9.1$ and $B_2^2/B_0^0 = 4.55$); Profile and top views of the conic structure with Cassini oval cross sections showing radial dependence. Note that a rectangular prism with half widths $\Delta_x = 5$ and $\Delta_y = \Delta_z = 9$ has almost same values of B_2^0/B_0^0 and B_2^2/B_0^0 ; thus for large altitudes its WTMM are equivalent in shape, but there is a factor in amplitudes because the rectangular prism has $B_0^0 = 8\Delta_x\Delta_y\Delta_z = 3240 > 400\pi$. See color version of this figure at back of this issue.

about vertical eccentricity (limit of $\frac{26}{5}B_2^2/B_0^0 = \frac{13}{25}(2\Delta_z^2 - \Delta_x^2 - \Delta_y^2)$) (Figure 7).

3.4. Analytic and Tensor Wavelet Coefficients

[31] Let us again consider the vertical component of gravity, g_z , analyzed using the analytic signal $A_1(\mathbf{b}, z + a)$ defined in equations (12) and (18), we obtain its analytic wavelet coefficients:

$$\mathcal{W}_{\Psi_A|g_z}(\mathbf{b}, a) = a[\mathbf{x}V_{xz}(\mathbf{b}, z_a) + \mathbf{y}V_{yz}(\mathbf{b}, z_a) + i\mathbf{z}V_{zz}(\mathbf{b}, z_a)], \quad (27)$$

where $V_{ij}(\mathbf{b}, z_a)$ is the gravity tensor at level $z_a = z_0 + a$ (Appendix B).

[32] Similarly, the tensor wavelet transform of g_z is

$$\mathcal{W}_{\Psi_T^2|g_z}(\mathbf{b}, a) = a^2 V_{ijz}(\mathbf{b}, z_a), \quad (28)$$

where $V_{ijz}(\mathbf{b}, z_a)$ is the vertical derivative of the gravity tensor at level $z_a = z + a$ (Appendix B).

[33] Using multipolar expansions for high altitudes, we obtain for both the analytic and tensor wavelet modulus

maxima, a vertical maximum line directly above the bary-center of source at $x = 0$. Wavelet moduli along maxima verify an expansion in the form of equation (20), where $C_2 = 0$, and $C_0 = 60$ (analytic wavelet) or $C_0 = 30/11$ (tensor wavelet). Thus the function S_2 (equation (23)) converges to $60B_2^0/B_0^0$ (analytic wavelet) or $\frac{30}{11}B_2^0/B_0^0$ (tensor wavelet). In practice, one can use one of these wavelet coefficients to locate an extended source of finite size and determine the ratio of B_2^0/B_0^0 ; then the value of B_2^2/B_0^0 can be estimated from horizontal wavelet coefficients by adjusting azimuthal variations according to equation (26).

3.5. Application to Magnetic Fields

[34] Let us now consider the magnetic total field anomaly δT . It is classically related to the 3×3 tensor \mathbf{V} of the newtonian potential [Okabe, 1979] by

$$\delta T(\mathbf{h}, z) = \mathbf{f}'[\mathbf{V}\mathbf{m}](\mathbf{h}, z), \quad (29)$$

where \mathbf{f} is the unit vector of normal magnetic field direction (related to normal declination D_n and inclination I_n by $f_x = \cos I_n \cos D_n$, $f_y = \cos I_n \sin D_n$, and $f_z = \sin I_n$), \mathbf{m} is the source magnetization vector (related to the source intensity $|m|$, its declination D and inclination I by $m_x = |m| \cos I \cos D$, $m_y = |m| \cos I \sin D$, and $m_z = |m| \sin I$).

[35] Its wavelet coefficients can be determined similarly to those of a gravity anomaly by derivative and upward continuation. Thus the analytic wavelet coefficient is

$$\mathcal{W}_{\Psi_A|\delta T}(\mathbf{b}, a) = a \sum_{k \in \{x, y, z\}} \mathbf{f}'[\mathbf{V}_k \mathbf{m}](\mathbf{b}, z_a) \mathbf{e}_k, \quad (30)$$

where \mathbf{e}_k is the unit vector as follows: $\mathbf{e}_x = \mathbf{x}$, $\mathbf{e}_y = \mathbf{y}$, and $\mathbf{e}_z = i\mathbf{z}$.

[36] Such a general expression can be used to explore the behavior of wavelet coefficients with any normal field direction, \mathbf{f} , and independent source magnetization, \mathbf{m} , using the multipolar expansion of tensor V_{ijk} and its combination $f_j m_i V_{ijk}$. However, let us simplify expressions using the classical approximation of normal magnetization direction ($\mathbf{m} = |m|\mathbf{f}$) and the pole-reduced total field anomaly $\delta T = |m|V_{zz}$ [Blakely, 1996]. Thus equation (30) reduces to

$$\mathcal{W}_{\Psi_A|\delta T_{pole}}(\mathbf{b}, a) = a|m| \sum_{k \in \{x, y, z\}} V_{zzk}(\mathbf{b}, z_a) \mathbf{e}_k. \quad (31)$$

Like in gravity, we can analyze modulus maxima caused by an isolated extended source using a multipolar expansion (calculations are similar to that shown in Appendix C). Using multipolar series, analytic wavelet modulus maxima can be shown to be located above $x = y = 0$, and their amplitudes $|\mathcal{W}_{\Psi_A|}(a)|$ verify a multipolar expansion in the form of equation (20), where $K = 6|m|$, $C_0 = 5/2$ and $C_2 = 0$.

4. Small Application to Real Data

[37] We show a preliminary application to real data, which is kept small for the aim of conciseness of the paper. We consider aeromagnetic data from a survey previously presented in our paper on the application to magnetic profiles using analytic wavelets [Sailhac et al., 2000]. We refer the reader to this paper for details on this survey and the geology of French Guyana. Now, let us only show a zoom of the geological sketch and the aeromagnetic map of the total field anomaly (Figure 8), and let us analyze only

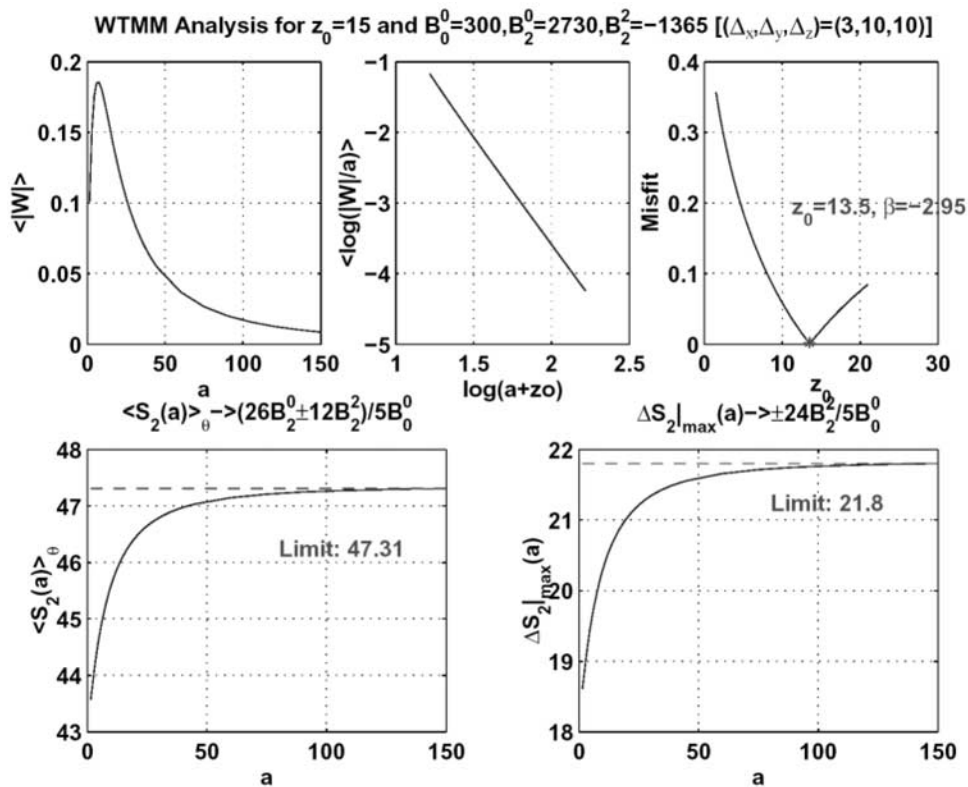


Figure 7. Scaling laws corresponding to the example shown on Figure 6. (a) Variation of the wavelet modulus with respect to dilation a . (b) Curve shown in Figure 7a becomes quasi-linear when properly rescaled and plotted in a log-log diagram. (c) Curve showing the discrepancy between rescaled curves as shown in Figure 7b and their best fitted straight lines for trial source depths $0 < z_0 < 22$. (d) Convergence of the azimuthal mean of $S_2(a)$. (e) Convergence of the difference $\Delta S_2(a) = \max S_2 - \min S_2$. See color version of this figure at back of this issue.

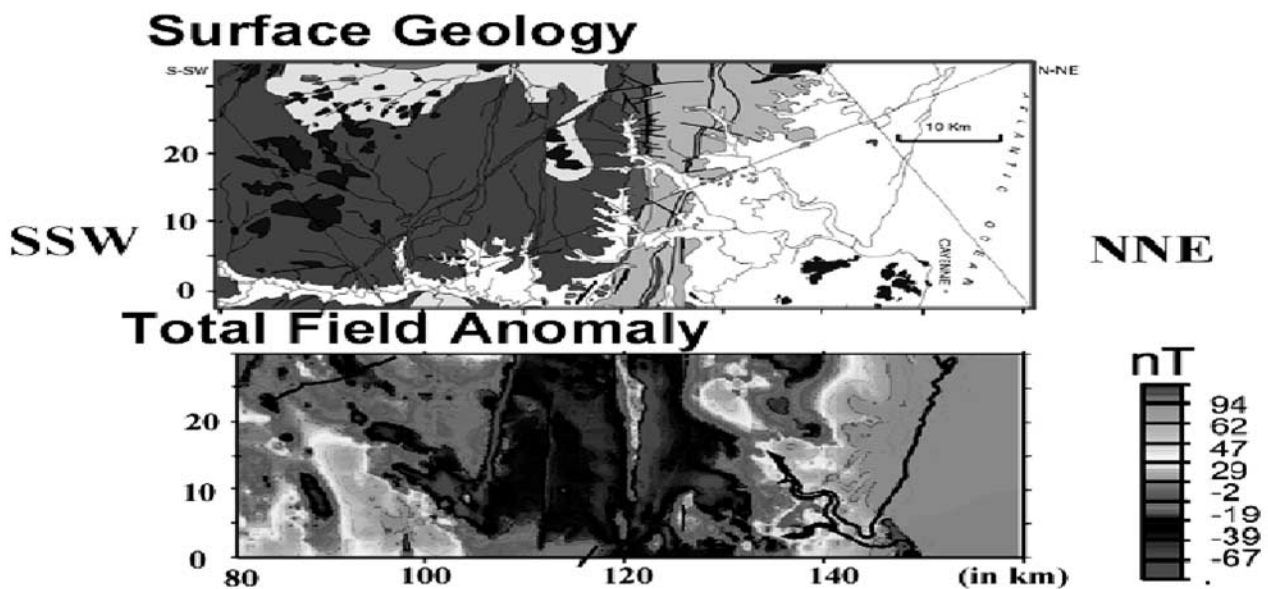


Figure 8. Data in French Guyana: Geological sketch and aeromagnetic map in SSW-NNE direction (see *Sailhac et al.* [2000] for geologic formations and reference coordinates). See color version of this figure at back of this issue.

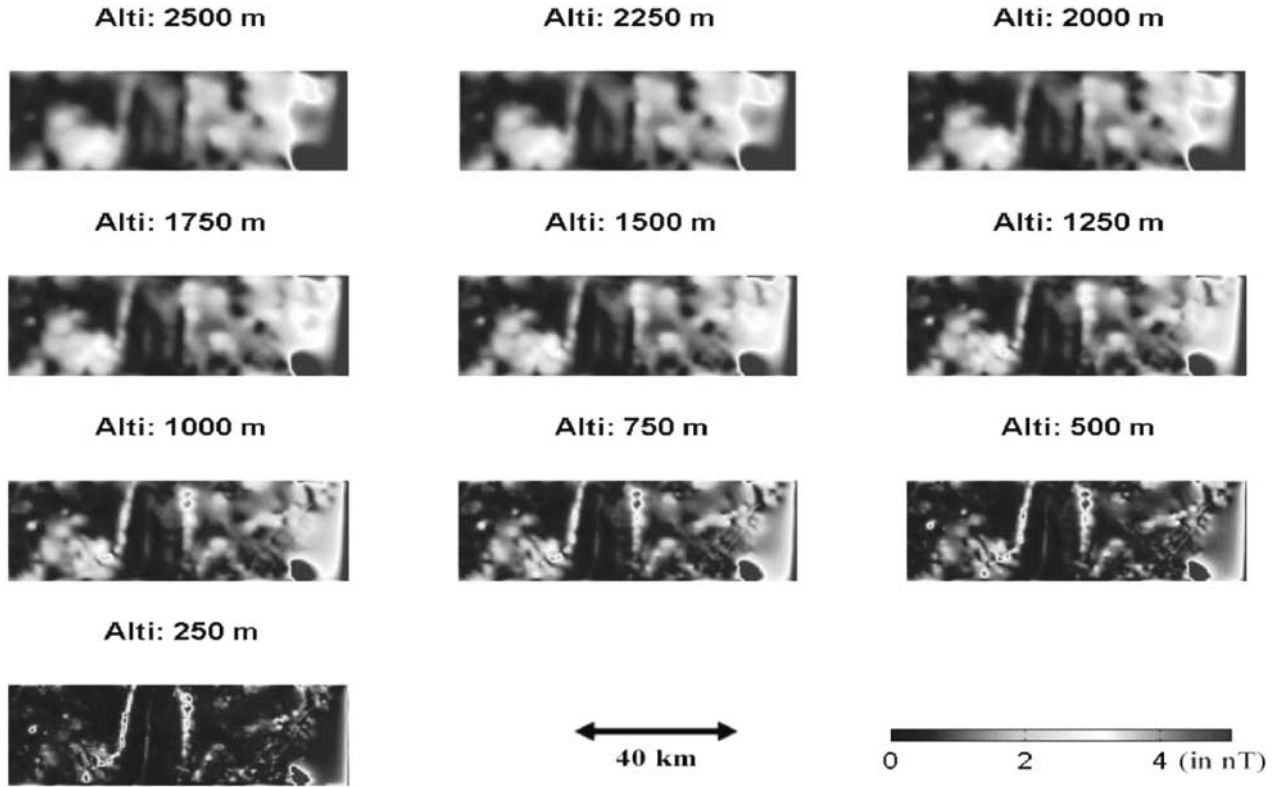


Figure 9. Wavelet transform of aeromagnetic map in Figure 8. Analytic wavelet coefficients (in nT) at various altitudes from 250 m up to 2500 m (each map is 80 km SSW by 30 km NNE). See color version of this figure at back of this issue.

one anomaly related to a sedimentary lens (Orapu series) which geometry in depth remains unexplored.

[38] Let us consider analytic wavelet coefficients computed from equation (30) that show the 3-D analytic signal upward continued to a series of altitudes (Figure 9). We may have considered another wavelet, but this choice allows modulus maxima of the anomalies to be located along the vertical to each source. The clear elongated structures present on the map at 250-m altitude are the SSW dike, central dike and the fault previously analyzed from aeromagnetic profiles of *Sailhac et al.* [2000]. As the altitude increases, other anomalies become prominent; for instance at the South head of the SSW dike, it could be associated to the coarse source of elongated dikes. Note that the large anomaly spread over the right side of the maps (NNE) is an artefact related to the strong anthropic magnetic anomaly over the city of Cayenne and to data extrapolation over offshore areas.

[39] Let us concentrate on the isolated anomaly shown in Figure 10 which size in $x \times y$ directions is 3 km \times 9 km. We associate this anomaly to the sandstone and quartzite Orapu complex (blue in the geological map of Figure 8) that has been emplaced in pull-apart basins [Ledru et al., 1991] and contains heavy minerals of significant magnetic signature [Vinchon, 1989]. White dots show the location of wavelet modulus maxima over the anomaly: They present a spreading below 500 meter altitude, above they are concentrated. Among these white dots, we consider the values of modulus maximum at each altitude $|\mathcal{W}(a)|$ and apply scaling rules

from equations (16) and (23). The first scaling rule (assuming homogeneous source) provides the depth and shape parameters $z_0 \approx 2400$ m and $\alpha \approx -3$ (straight line in red, with slope $\beta = -4$); then the second-order scaling rule (assuming that the source is extended with a finite size) provides the parameter $S_2(\infty) = C_0 B_2^0 / B_0^0 \approx -15$ km² (limit of the square size function $S_2(a)$) where $C_0 = 5/2$ (see equation (31)). By using Table 1, we can convert this $S_2(\infty)$ to the vertical dimension Δ_3 of the source. For this, let us assume its horizontal sizes ($\Delta_1 = 3$ km and $\Delta_2 = 9$ km from the geological map) and a typical geometry: either a triaxial ellipsoid or a rectangular prism. In the first case, we obtain $\Delta_3^2 = 2S_2(\infty) + [(\Delta_1^2 + \Delta_2^2)/2] \approx 15$ km², and in the second case $\Delta_3^2 = \frac{6}{5}S_2(\infty) + [(\Delta_1^2 + \Delta_2^2)/2] \approx 27$ km². Finally, we can interpret Δ_3 estimates combined with the depth estimate of 2400m, and say that this sedimentary cell probably extends over depths of 0–500 m to 3500–5000 m.

5. Conclusion and Perspectives

[40] The wavelet technique is aimed at analyzing both the location and geometry of the sources of potential fields via relations of derivatives of the upward continued field. This can be applied to any potential fields with scalar, vector or tensor values. The potential field wavelet domain shows symmetries to the underground sources in complex geometrical features that depend on the choice of wavelet order and directions. However, some combinations classically used in potential field interpretation, like the analytic signal,

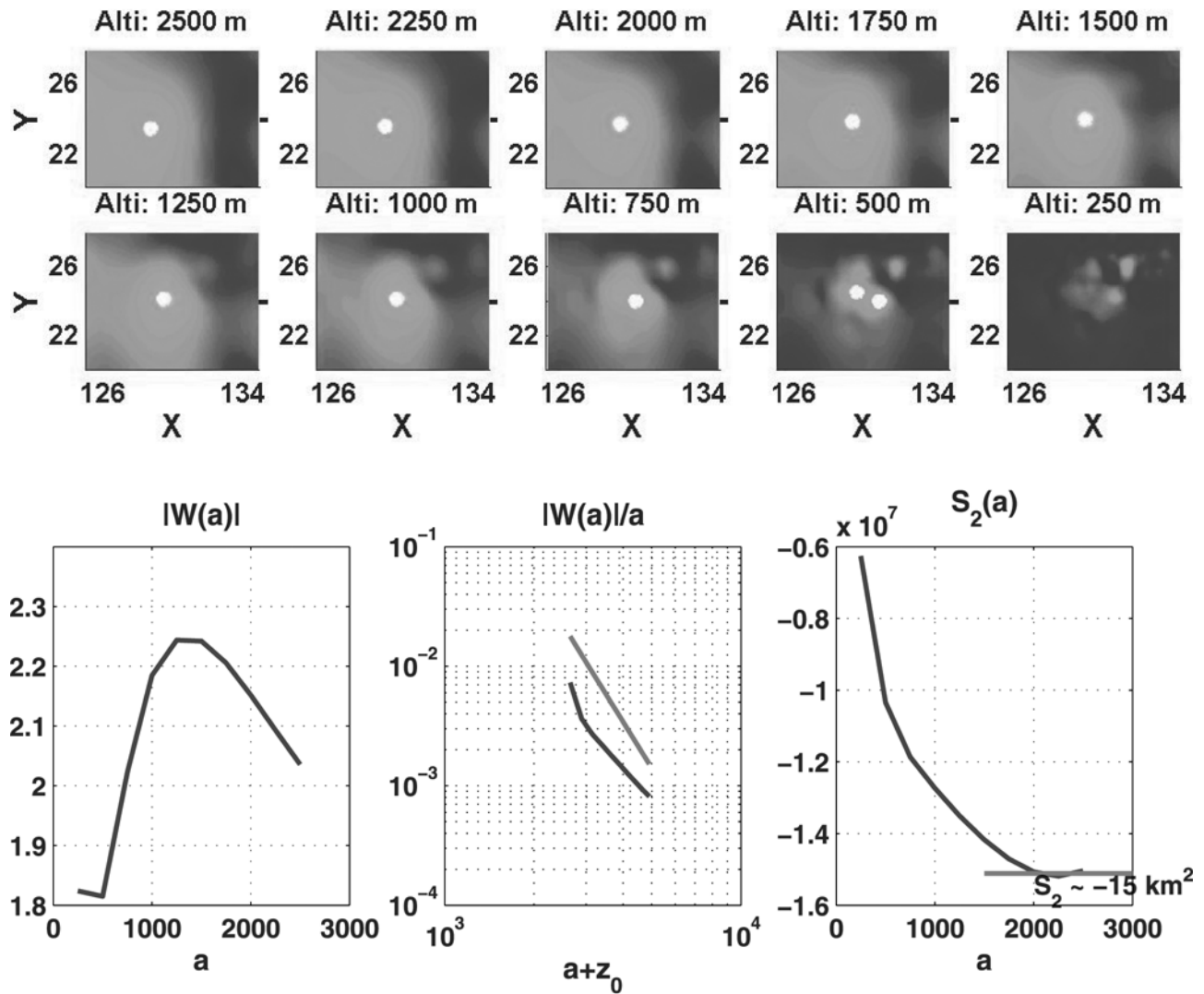


Figure 10. Interpretation of the wavelet transform modulus maxima of the aeromagnetic map in Figure 8. (top) Zoom (with same color scale as in Figure 9) of an area of $10 \text{ km} \times 8 \text{ km}$ where modulus maxima concentrate (white dots). (bottom) Interpretation functions based upon scaling of modulus maxima $|W|$: the log-log curve of $|W/a|$ for the depth estimation and the square function S_2 for the sizes. See color version of this figure at back of this issue.

exhibit more simple behaviors of the wavelet modulus that can be used to estimate depth and sizes of 3-D sources. An automatic depth to source determination is based upon adjustments of a scaling law for the modulus of complex wavelet coefficients (of $|W_a|/a^\gamma$ versus $a + z_0$). This can be applied for some nonlocal sources where residuals of a power scaling law form new quantities “ S_2 ” related to the first moments of the source by an equation with parameters depending on the type of source (either a triaxial ellipsoid or a rectangular prism, etc.).

[41] Multipolar series expansion were first introduced in potential field interpretation by *Grant and West* [1965], but did not appear to be useful until now. The wavelet modulus maxima approach involves that the first multipolar moments B_0^0 , B_2^0 and B_2^2 , could be helpful to generalize interpretations, for local homogeneous sources like in Euler deconvolution then to more general extended sources. The first assumption of local homogeneous source allows estimation of the

source depths, and is limited to sources with well localized sharp singularity. Then the use of S_2 involves the assumption of a soft localization of the source, and one can go further by additional information on its geometry, for example by assuming prismatic or ellipsoidal shapes, and possibly complex heterogeneous structures having similar combinations of their first moments.

[42] Two-dimensional applications of this approach have been shown in previous publications to be effective; the small application of this 3-D generalization to the estimation of the depth extent of a sedimentary lens from the Orapu series in French Guyana opens new perspectives. The key point of this technique is to convert potential field wavelet domain into underground source properties. This helps in the interpretation of potential field maps by providing size estimations where a number of classical techniques like the Euler deconvolution would propose only depth estimates. Besides, the additional information that is added to convert

the quantity S_2 into the first moments and the sizes of the source contains part of the ambiguity of the potential field inversion. We expect that this possibility of adding this information during the last stage of the procedure (once homogeneous sources have been determined) opens new perspectives in potential field interpretations.

Appendix A: Formulae Used in Figures

[43] Let us give formulae used to plot wavelet coefficients in Figures 3 and 4 that correspond to different sources and the resulting gravity field g_z analyzed using the wavelet ψ_x^2 . For Figure 3, formulae are similar to those reported by *Hammer* [1971]. For Figure 4, formulae follow derivatives of the potential caused by a polyhedral body as shown by *Okabe* [1979]. In these relations, \mathbf{h} is the horizontal coordinate vector $(x, y)^t$, z_0 is the depth to the source singularity, and a is the dilation (i.e., altitude of upward continuation).

[44] Wavelet coefficients in Figure 3a are (point source)

$$\mathcal{W}_{\psi_x^2|g_z}(\mathbf{h}, a) = \frac{3}{2\pi} a^2 z_a \frac{3x^2 - h^2 - z_a^2}{(h^2 + z_a^2)^{3.5}}. \quad (\text{A1})$$

Wavelet coefficients in Figure 3b are (horizontal line in y)

$$\mathcal{W}_{\psi_x^2|g_z}(\mathbf{h}, a) = \frac{1}{\pi} a^2 z_a \frac{3x^2 - z_a^2}{(x^2 + z_a^2)^3}. \quad (\text{A2})$$

Wavelet coefficients in Figure 3c are (vertical line)

$$\mathcal{W}_{\psi_x^2|g_z}(\mathbf{h}, a) = -\frac{3}{2\pi} a^2 z_a \frac{x}{(h^2 + z_a^2)^{2.5}}. \quad (\text{A3})$$

Wavelet coefficients in Figure 3d are (vertical strip in y)

$$\mathcal{W}_{\psi_x^2|g_z}(\mathbf{h}, a) = -\frac{2}{\pi} a^2 z_a \frac{x}{(x^2 + z_a^2)^2}. \quad (\text{A4})$$

Wavelet coefficients in Figure 3e are (vertical step in y)

$$\mathcal{W}_{\psi_x^2|g_z}(\mathbf{h}, a) = \frac{1}{\pi} a^2 z_a \frac{1}{(x^2 + z_a^2)^2}. \quad (\text{A5})$$

[45] Wavelet coefficients in Figure 4 are (semi-infinite rectangular prism source at $x = \pm 10$, $y = \pm 10$ and depth of the top $z_0 = 1$)

$$\mathcal{W}_{\psi_x^2|g_z}(\mathbf{h}, a) = -a^2 \sum_{k=1}^4 s_k \frac{x'_k}{r'_k (y'_k + r'_k)}, \quad (\text{A6})$$

where the index k runs over the four corners of the rectangle with coordinate vector $\mathbf{r}_k = (x_k, y_k, z_0)^t$, the wavelet coefficient is at an observation point with coordinate vector $\mathbf{r} = (\mathbf{h}^t, -a)^t = (x, y, -a)^t$, relative coordinates are $\mathbf{r}'_k = \mathbf{r}_k - \mathbf{r}$, and the sign parameter is defined from the signs of horizontal coordinates $s_k = \text{sign}(x'_k) \text{sign}(y'_k)$.

Appendix B: Multipole Expansion of Upward Continued Fields

[46] Let us give multipole expansion of potential fields, on the basis of successive derivatives of equation (17). For simplicity of equations, we assume bodies which principal axes (x', y', z') are parallel to the survey axes (x, y, z) . Thus in applications, it may be necessary to consider coordinate

rotation or looking for some invariant under rotation [*Grant and West*, 1965; *Pedersen and Rasmussen*, 1990; *Dransfield*, 1994].

[47] The following expressions are given for an observation point at level $z_a = z + a$, at large distance $r = \sqrt{x^2 + y^2 + z_a^2}$ from the source whose center is at $x = 0$, $y = 0$, and $z = -z_0$. The gravity potential $V(x, y, z_a)$ verifies

$$V(x, y, z_a) \approx \frac{-B_0^0}{r} + B_2^0 \frac{r^2 - 3z_a^2}{2r^5} + B_2^0 \frac{3(y^2 - x^2)}{r^5}. \quad (\text{B1})$$

The three components of the gravity vector $\mathbf{g} = (g_x, g_y, g_z)^t$ are such that

$$\begin{aligned} g_x(x, y, z_a) &\approx B_0^0 \frac{x}{r^3} + B_2^0 \frac{-3x(r^2 - 5z_a^2)}{2r^7} + B_2^0 \frac{3x(5(x^2 - y^2) - 2r^2)}{r^7}, \\ g_y(x, y, z_a) &\approx B_0^0 \frac{y}{r^3} + B_2^0 \frac{-3y(r^2 - 5z_a^2)}{2r^7} + B_2^0 \frac{3y(5(x^2 - y^2) + 2r^2)}{r^7}, \\ g_z(x, y, z_a) &\approx B_0^0 \frac{-z_a}{r^3} + B_2^0 \frac{3z_a(3r^2 - 5z_a^2)}{2r^7} + B_2^0 \frac{15z_a(y^2 - x^2)}{r^7}. \end{aligned} \quad (\text{B2})$$

[48] The gravity tensor $V_{ij}(x, y, z_a)$ verifies

$$\begin{aligned} V_{xz}(x, y, z_a) &\approx B_0^0 \frac{3xz_a}{r^5} + B_2^0 \frac{15xz_a(7z_a^2 - 3r^2)}{2r^9} \\ &\quad + B_2^0 \frac{15xz_a(7x^2 - 7y^2 - 2r^2)}{r^9}, \\ V_{yz}(x, y, z_a) &\approx B_0^0 \frac{3yz_a}{r^5} + B_2^0 \frac{15yz_a(7z_a^2 - 3r^2)}{2r^9} \\ &\quad + B_2^0 \frac{15yz_a(7x^2 - 7y^2 + 2r^2)}{r^9}, \\ V_{zz}(x, y, z_a) &\approx B_0^0 \frac{3z_a^2 - r^2}{r^5} + B_2^0 \frac{3(35z_a^4 - 30z_a^2r^2 + 3r^4)}{2r^9} \\ &\quad + B_2^0 \frac{15(x^2 - y^2)(7z_a^2 - r^2)}{r^9}, \\ V_{xy}(x, y, z_a) &\approx B_0^0 \frac{-3xy}{r^5} + B_2^0 \frac{15xy(r^2 - 7z_a^2)}{2r^9} + B_2^0 \frac{105xy(y^2 - x^2)}{r^9}, \end{aligned} \quad (\text{B3})$$

where the remaining components are obtained by permuting the x, y, z indices.

[49] Higher-order derivatives of the gravity tensor $V_{ijk}(x, y, z_a)$ verify

$$\begin{aligned} V_{xxx}(h, z_a) &\approx B_0^0 \frac{3x(r^2 - z_a^2)}{r^7} + B_2^0 \frac{45x(21z_a^4 + 14z_a^2r^2 - r^4)}{2r^{11}} \\ &\quad + B_2^0 \frac{15x(7(x^2 - y^2)(r^2 - 9z_a^2) + 2r^2(7z_a^2 - r^2))}{r^{11}}, \\ V_{yzz}(h, z_a) &\approx B_0^0 \frac{3y(r^2 - z_a^2)}{r^7} + B_2^0 \frac{45y(21z_a^4 + 14z_a^2r^2 - r^4)}{2r^{11}} \\ &\quad + B_2^0 \frac{15y(7(x^2 - y^2)(r^2 - 9z_a^2) - 2r^2(7z_a^2 - r^2))}{r^{11}}, \\ V_{zzz}(h, z_a) &\approx B_0^0 \frac{3z_a(5z_a^2 - 3r^2)}{r^7} + B_2^0 \frac{3z_a(-63z_a^4 + 90z_a^2r^2 - 17r^4)}{2r^{11}} \\ &\quad + B_2^0 \frac{315z_a(x^2 - y^2)(r^2 - 3z_a^2)}{r^{11}}, \\ V_{xyz}(h, z_a) &\approx B_0^0 \frac{15xyz_a}{r^7} + B_2^0 \frac{15.21xyz_a(3z_a^2 - r^2)}{2r^{11}} \\ &\quad + B_2^0 \frac{15.21.3xyz_a(x^2 - y^2)}{r^{11}}, \end{aligned} \quad (\text{B4})$$

the other components being obtained by permuting the x, y, z indices.

Appendix C: Horizontal Wavelet Coefficients

[50] Here we show relations of horizontal gradient wavelet coefficients of the vertical gravity anomaly with properties of 3-D sources of constant density where parameters B_2^0 and B_2^2 are not identically zero (see Table 1).

[51] First, let us assume cylindrical symmetry, where horizontal sizes Δ_1 and Δ_2 are equal and can differ to the vertical size Δ_3 . Here, we have $B_2^0 \neq 0$ and $B_2^2 = 0$. The horizontal gradient wavelet coefficients as introduced by Hornby *et al.* [1999] are given in equation (25) with series expansion given in equation (B3). From cylindrical symmetry, which implies $B_2^2 = 0$, this can be simplified at large distance $r = \sqrt{\rho^2 + z_a^2}$, where $\rho = \sqrt{x^2 + y^2}$ and $z_a = z_0 + a$:

$$\mathcal{W}_{\psi_{G|g_z}}(x, y, a) = \frac{3B_2^0 a z_a \rho}{r^5} \left(1 + 10 \frac{B_2^0 z_a^2 - \frac{3}{4} \rho^2}{B_0^0 r^4} \right). \quad (C1)$$

Deriving equation (C1) along ρ^2 yields the condition which defines the modulus maxima of the horizontal wavelet coefficients:

$$(z_a^2 - 4\rho^2)(z_a^2 + \rho^2)^2 = -10 \frac{B_2^0}{B_0^0} \left(z_a^4 - \frac{41}{4} z_a^2 \rho^2 + \frac{9}{2} \rho^4 \right). \quad (C2)$$

Let us introduce the constant $\gamma_0 = 10B_2^0/B_0^0$, which dimension is the square of a distance and relates to the difference between horizontal and vertical distances (see Table 1). When $\gamma_0 = 0$ (or $B_2^0 = 0$), equation (C2) simplifies to the homogeneous case with solution $z_a^2 = 4\rho^2$, which defines a cone with center ($\rho = 0$, $z_a = 0$): at each altitude a , modulus maxima are located on a circle with radius $\rho = (z_0 + a)/2$. This can be seen as the solution with zeroth order expansion in γ_0/z_a^2 . Let us now consider the first order expansion, with solutions in the form

$$\rho^2 = \frac{z_a^2}{4} \left[1 + C \frac{\gamma_0}{z_a^2} + O\left(\frac{\gamma_0^2}{z_a^4}\right) \right], \quad (C3)$$

where C is a constant to be found. Rewriting equation (C2) at the first-order expansion in γ_0/z_a^2 reads

$$-\frac{25}{16} C \gamma_0 z_a^4 \left[1 + O\left(\frac{\gamma_0}{z_a^2}\right) \right] = -\gamma_0 z_a^4 \left[-\frac{41}{32} + O\left(\frac{\gamma_0}{z_a^2}\right) \right], \quad (C4)$$

which yields $C = -41/50$. Thus modulus maxima are located on circles with square radius $\rho^2 \approx z_a^2/4 - \frac{41}{20} B_2^0/B_0^0$. For large altitudes (where $z_a^2 \gg B_2^0/B_0^0$) they define a cone which top is at $a \approx -z_0$; at smaller altitudes, the cone is bent and has either a larger radius (if $B_2^0 < 0$) or a smaller radius (if $B_2^0 \geq 0$) in which case the top can be moved up to $a \approx -z_0 + \sqrt{41B_2^0/5B_0^0}$. Furthermore, this yields a possible application to the interpretation of the observed radius ρ of modulus maxima as a function of altitudes a , to estimate both the parameter $B_2^0 \neq 0$ and the depth z_0 : A series of depth z_0 can be tested by linear regressions of ρ^2 versus $z_a^2 = (z_0 + a)^2$; the regression with minimum misfit provides the depth z_0 and the y intercept $-\frac{41}{20} B_2^0/B_0^0$.

[52] Let us now release the condition for cylindrical symmetry ($B_2^2 \neq 0$). Similarly to the previous case, we search for the first-order expansion in both γ_0/z_a^2 and γ_2/z_a^2 where $\gamma_0 = 10B_2^0/B_0^0$ and $\gamma_2 = 10B_2^2/B_0^0$:

$$\rho^2 = \frac{z_a^2}{4} \left[1 + C_0 \frac{\gamma_0}{z_a^2} + C_2 \frac{\gamma_2}{z_a^2} + O\left(\frac{\gamma_0^2}{z_a^4}\right) + O\left(\frac{\gamma_2^2}{z_a^4}\right) \right], \quad (C5)$$

where C_0 and C_2 are ρ constants to be found. We use again cylindrical coordinates (where $x = \rho \cos\phi$ and $y = \rho \sin\phi$ such that $\rho^2 = x^2 + y^2$) and search for zeros of ρ derivatives, so we obtain the ridge of modulus maxima. With the help of Maple symbolic calculator, this gives $C_0 = -41/50$ and $C_2 = 31 \cos 2\phi/25$.

[53] Thus $\rho(\phi)$ is the polar equation of a Cassini oval, and the wavelet coefficient at modulus maxima lines (x^*, y^*, a) can be approximated at large altitude a such that $z_a^2 = (z_0 + a)^2 \gg \gamma_0$ and $z_a^2 = (z_0 + a)^2 \gg \gamma_2$ by

$$\left| \mathcal{W}_{\psi_{G|g_z}(\dots, 0)}(x^*, y^*, a) \right| \approx \frac{48B_2^0 a}{25\sqrt{5}z_a^3} \left[1 + \frac{13\gamma_0 - 6\gamma_2 \cos 2\phi}{25z_a^2} \right], \quad (C6)$$

which is equation (26).

[54] **Acknowledgments.** This paper benefited from comments made by Associated Editor Stephen Park and reviewer Misac Nabighian. We also had numerous discussions with our colleagues Pierre Keating and Ginette Saracco. This work benefited support from CNRS ACI "Eau, Sol et Environnement". This is EOST-IPGS contribution 2002.26-UMR7516.

References

- Baranov, W., *Potential Fields and Their Transformations in Applied Geophysics*, *Geophys. Monogr. Ser.*, vol. 6, 121 pp., Gebruder Borntraeger, Stuttgart, Germany, 1975.
- Bell, R. E., R. Anderson, and L. Pratson, Gravity gradiometry resurfaces, *Leading Edge*, 16, 55–59, 1997.
- Bhattacharyya, B. K., Design of spatial filters and their application to high-resolution aeromagnetic data, *Geophysics*, 37, 68–91, 1972.
- Biegert, E. K., and P. S. Millegan, Beyond recon: The new world of gravity and magnetics, *Leading Edge*, 17, 41–42, 1998.
- Blakely, R. J., *Potential Theory in Gravity and Magnetic Applications*, 441 pp., Cambridge Univ. Press., New York, 1996.
- Dransfield, M. H., Airborne gravity gradiometry, Ph.D. thesis, 254 pp., Univ. of West. Aust., Nedlands, Australia, 1994.
- Fedi, M., and A. Rapolla, 3-D inversion of gravity and magnetic data with depth resolution, *Geophysics*, 64, 452–460, 1999.
- Galdeano, A., Traitement des données aéromagnétiques: Méthodes et applications, thèse de doctorat, 153 pp., Univ. de Paris VI, Paris, 1974.
- Gibert, D., and A. Galdeano, A computer program to perform the upward continuation of potential field data, *Comput. Geosci.*, 11, 533–588, 1985.
- Gibert, D., and M. Pessel, Identification of sources of potential fields with the continuous wavelet transform: Application to self-potential profiles, *Geophys. Res. Lett.*, 28, 1863–1866, 2001.
- Grant, F. S., and G. F. West, *Interpretation Theory in Applied Geophysics*, McGraw-Hill, New York, 1965.
- Grauch, V. J. S., and P. S. Millegan, Mapping intrabasinal faults from high-resolution aeromagnetic data, *Leading Edge*, 17, 53–55, 1998.
- Hammer, S., Vertical attenuation of anomalies in airborne gravimetry, *Geophysics*, 36, 867–877, 1971.
- Hornby, P., F. Boschetti, and F. G. Horovitz, Analysis of potential field data in the wavelet domain, *Geophys. J. Int.*, 137, 175–196, 1999.
- Hsu, S.-K., D. Coppens, and C.-T. Shyu, Depth to magnetic source using the generalized analytic signal, *Geophysics*, 63, 1947–1957, 1998.
- Huang, D., Enhancement of automatic interpretation techniques for recognising potential field sources, Ph.D. thesis, 216 pp., Univ. of Leeds, Leeds, England, 1996.
- Ledru, P., J.-L. Lasserre, E. Manier, and D. Memier, Le Paleoproterozoïque nord-guyanaise: Révision de la lithologie, tectonique transcurrente et dy-

- namique des bassins sédimentaires, *Bull. Soc. Géol. Fr.*, 162, 627–636, 1991.
- Le Mouél, J.-L., Le levé aéromagnétique de la France: Calcul des composantes du champ à partir des mesures de l'intensité, *Ann. Géophys.*, 26, 229–258, 1970.
- Martelet, G., P. Sailhac, F. Moreau, and M. Diament, Characterization of geological boundaries using 1-D wavelet transform on gravity data: Theory and application to the Himalayas, *Geophysics*, 66, 1116–1129, 2001.
- Moreau, F., Méthodes de traitement de données géophysiques par transformée en ondelettes. thèse de doctorat, 177 pp., Univ. de Rennes I, Rennes, France, 1995.
- Moreau, F., D. Gibert, M. Holschneider, and G. Saracco, Wavelet analysis of potential fields, *Inverse Probl.*, 13, 165–178, 1997.
- Moreau, F., D. Gibert, M. Holschneider, and G. Saracco, Identification of sources of potential fields with the continuous wavelet transform: Basic theory, *J. Geophys. Res.*, 104, 5003–5013, 1999.
- Nabighian, M. N., Toward a three-dimensional automatic interpretation of potential field data via the generalized Hilbert transforms: Fundamental relations, *Geophysics*, 49, 780–786, 1984.
- Nabighian, M. N., and R. O. Hansen, Unification of Euler and Werner deconvolution in three dimensions via the generalized Hilbert transform, *Geophysics*, 66, 1805–1810, 2001.
- Nelson, J. B., Calculation of the magnetic gradient tensor from total field gradient measurements and its application to geophysical interpretation, *Geophysics*, 53, 957–966, 1988.
- Okabe, M., Analytic expressions for the gravity anomalies due to homogeneous polyhedral bodies and translations into magnetic anomalies, *Geophysics*, 44, 730–741, 1979.
- Paul, M. K., Quantitative interpretation of three dimensional finite mass distribution from gravity data, *Geofis. Pura Appl.*, 52, 28–46, 1961.
- Pedersen, L. B., and T. M. Rasmussen, The gradient tensor of potential fields anomalies: Some implications on data collection and data processing of maps, *Geophysics*, 55, 1558–1566, 1990.
- Pilkington, M., 3-D magnetic imaging using conjugate gradients, *Geophysics*, 62, 1132–1142, 1997.
- Ravat, D., and P. T. Taylor, Determination of depths to centroids of three-dimensional sources of potential-field anomalies with examples from environmental and geological applications, *J. Appl. Geophys.*, 39, 191–208, 1998.
- Reid, A. B., J. M. Allsop, H. Grasner, A. J. Millet, and I. W. Somerton, Magnetic interpretation in three dimensions using Euler deconvolution, *Geophysics*, 55, 80–91, 1990.
- Roest, W. R., J. Verhoef, and M. Pilkington, Magnetic interpretation using the 3-D analytic signal, *Geophysics*, 57, 116–125, 1992.
- Sailhac, P., and G. Marquis, Analytic potentials for the forward and inverse modeling of SP anomalies caused by subsurface fluid flow, *Geophys. Res. Lett.*, 28, 1851–1854, 2001.
- Sailhac, P., A. Galdeano, D. Gibert, F. Moreau, and C. Delor, Identification of sources of potential fields with the continuous wavelet transform: Complex wavelets and applications to magnetic profiles in French Guiana, *J. Geophys. Res.*, 105, 19,455–19,475, 2000.
- Silva, J. B. C., V. C. F. Barbosa, and W. E. Medeiros, Scattering, symmetry, and bias analysis of source-position estimates in Euler deconvolution and its practical implications, *Geophysics*, 66, 1149–1156, 2001.
- Tarantola, A., and B. Valette, Inverse Problems = Quest for Information, *J. Geophys.*, 50, 159–170, 1982.
- Thompson, D. T., EULDPH: A new technique for making computer-assisted depth estimates from magnetic data, *Geophysics*, 47, 31–37, 1982.
- Vinchon, C., Nouvelles hypothèses sur les contrôles sédimentologiques des gîtes aurifères dans les séries gréso-conglomératiques du Witwatersrand (Afrique du Sud), du Tarkwaïen (Afrique de l'Ouest) et de l'Orapu (Guyane Française), *Chron. Rech. Min.*, 497, 115–130, 1989.

D. Gibert, Géosciences Rennes (UMR 6118), CNRS and Université Rennes 1, Bât. 15, Campus de Beaulieu, F-35042 Rennes Cedex, France. (dominique.gibert@univ-rennes1.fr)

P. Sailhac, Laboratoire de Proche Surface (CNRS, UMR 7516), EOS-IMPS, 5 rue René Descartes, F-67084 Strasbourg Cedex, France. (pascal.sailhac@eost.u-strasbg.fr)

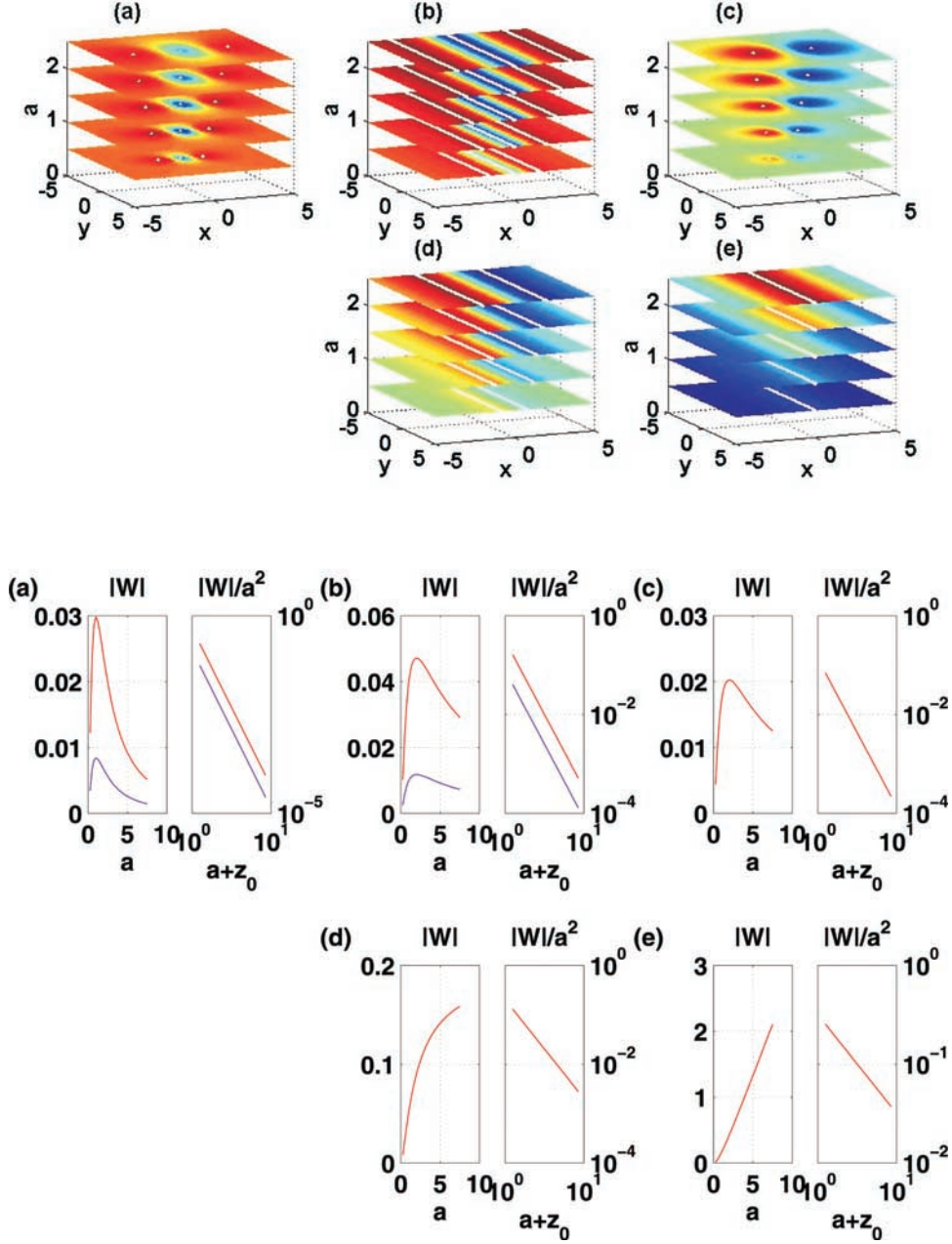


Figure 3. Typical scaling relations of the potential field wavelet modulus maxima for local homogeneous sources following to functions shown in Figure 2 and translated to the depth $z = z_0$ (Figures 3a–3e correspond to Figures 2a–2e). We show both the 3-D skeleton (top in white) and the log-log plots of the normalized amplitudes $|\mathcal{W}_a|/a^\gamma$ versus translated altitudes $a + z_0$ (bottom). In this figure, we only consider the case of vertical gravity fields analyzed with the second-order $\psi_{\mathbf{x}}^2(\mathbf{h})$ wavelet defined in equation (7) and cone-like structures appear in xz sections.

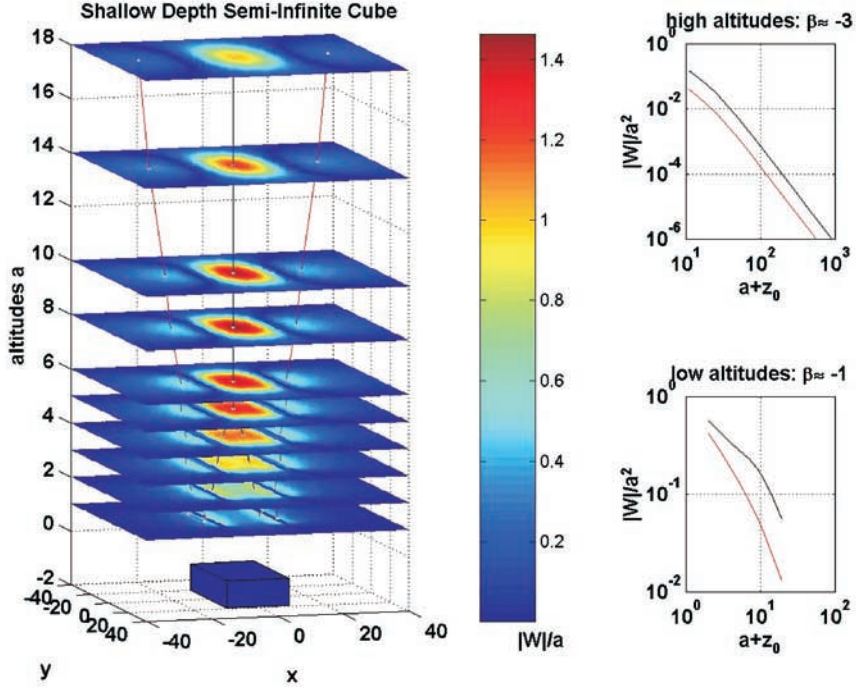


Figure 4. Different regions of potential field wavelet domain of extended sources: The gravity case of a rectangular prism of finite horizontal sizes $\Delta_1 = \Delta_2 = 10$ and semi-infinite height which top is relatively shallow, at $z_0 = 1$ (bottom left). Because of the source size, wavelet modulus maxima of the 3-D skeleton (left) exhibit different homogeneity behaviors depending on the region of focus (right): either at large altitudes (top right: $\beta \approx -3$, $\alpha \approx -2$), or at lower altitudes near to the border (bottom right: $\beta \approx -1$, $\alpha \approx 0$). We have used the wavelet $\psi_x^2(\mathbf{h})$ as in Figure 3.

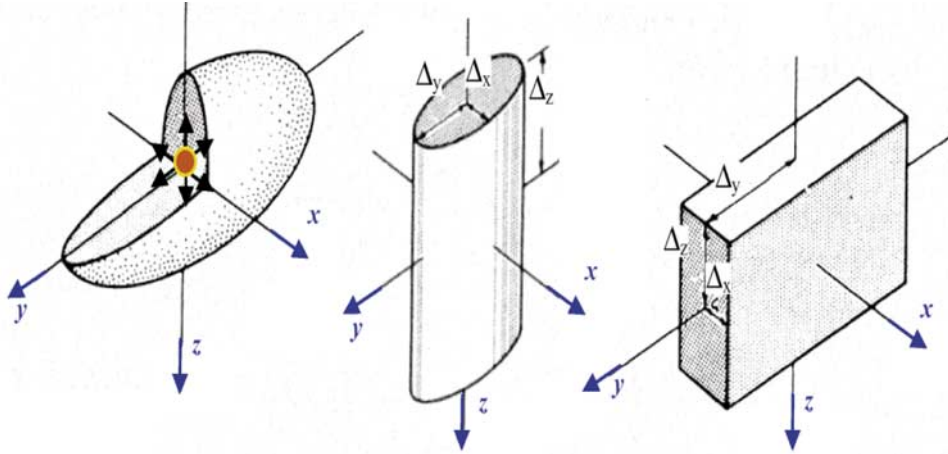


Figure 5. Examples of simple multipolar sources: Triaxial ellipsoid, cylinder, and rectangular prism.

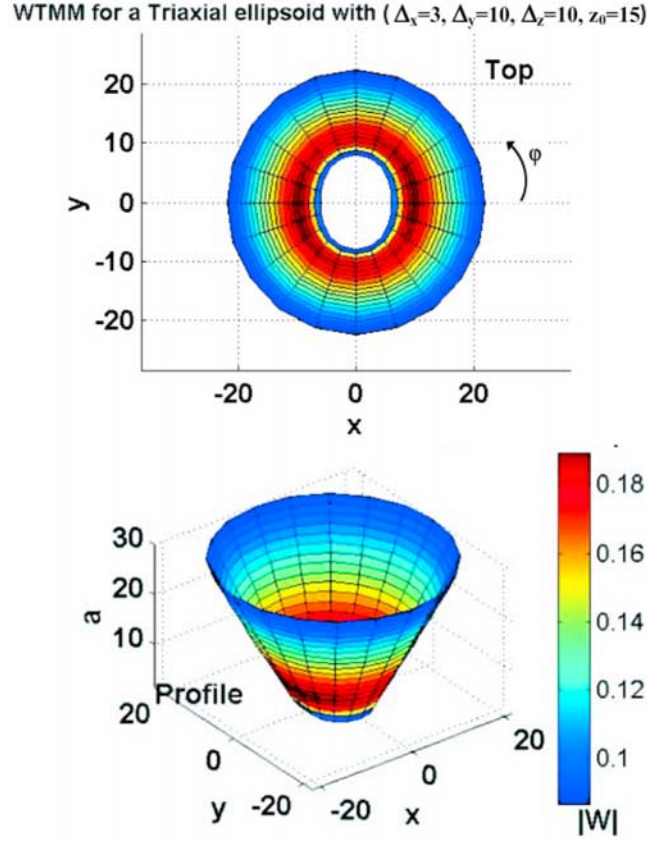


Figure 6. Wavelet transform modulus maxima (WTMM) for a triaxial ellipsoid with semiaxis values $\Delta_x = 3$, $\Delta_y = \Delta_z = 10$, and $z_0 = 15$ ($B_0^0 = \frac{4}{3}\pi\Delta_x\Delta_y\Delta_z = 400\pi$, $B_2^0/B_0^0 = 9.1$ and $B_2^2/B_0^0 = 4.55$): Profile and top views of the conic structure with Cassini oval cross sections showing radial dependence. Note that a rectangular prism with half widths $\Delta_x = 5$ and $\Delta_y = \Delta_z = 9$ has almost same values of B_2^0/B_0^0 and B_2^2/B_0^0 ; thus for large altitudes its WTMM are equivalent in shape, but there is a factor in amplitudes because the rectangular prism has $B_0^0 = 8\Delta_x\Delta_y\Delta_z = 3240 > 400\pi$.

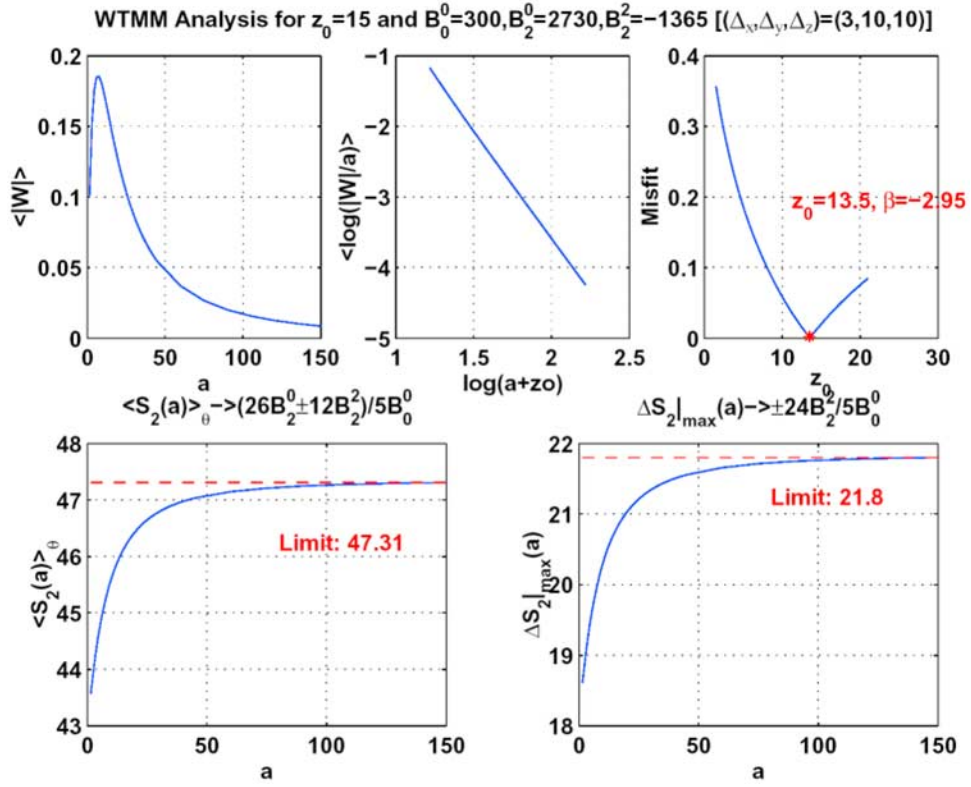


Figure 7. Scaling laws corresponding to the example shown on Figure 6. (a) Variation of the wavelet modulus with respect to dilation a . (b) Curve shown in Figure 7a becomes quasi-linear when properly rescaled and plotted in a log-log diagram. (c) Curve showing the discrepancy between rescaled curves as shown in Figure 7b and their best fitted straight lines for trial source depths $0 < z_0 < 22$. (d) Convergence of the azimuthal mean of $S_2(a)$. (e) Convergence of the difference $\Delta S_2(a) = \max S_2 - \min S_2$.

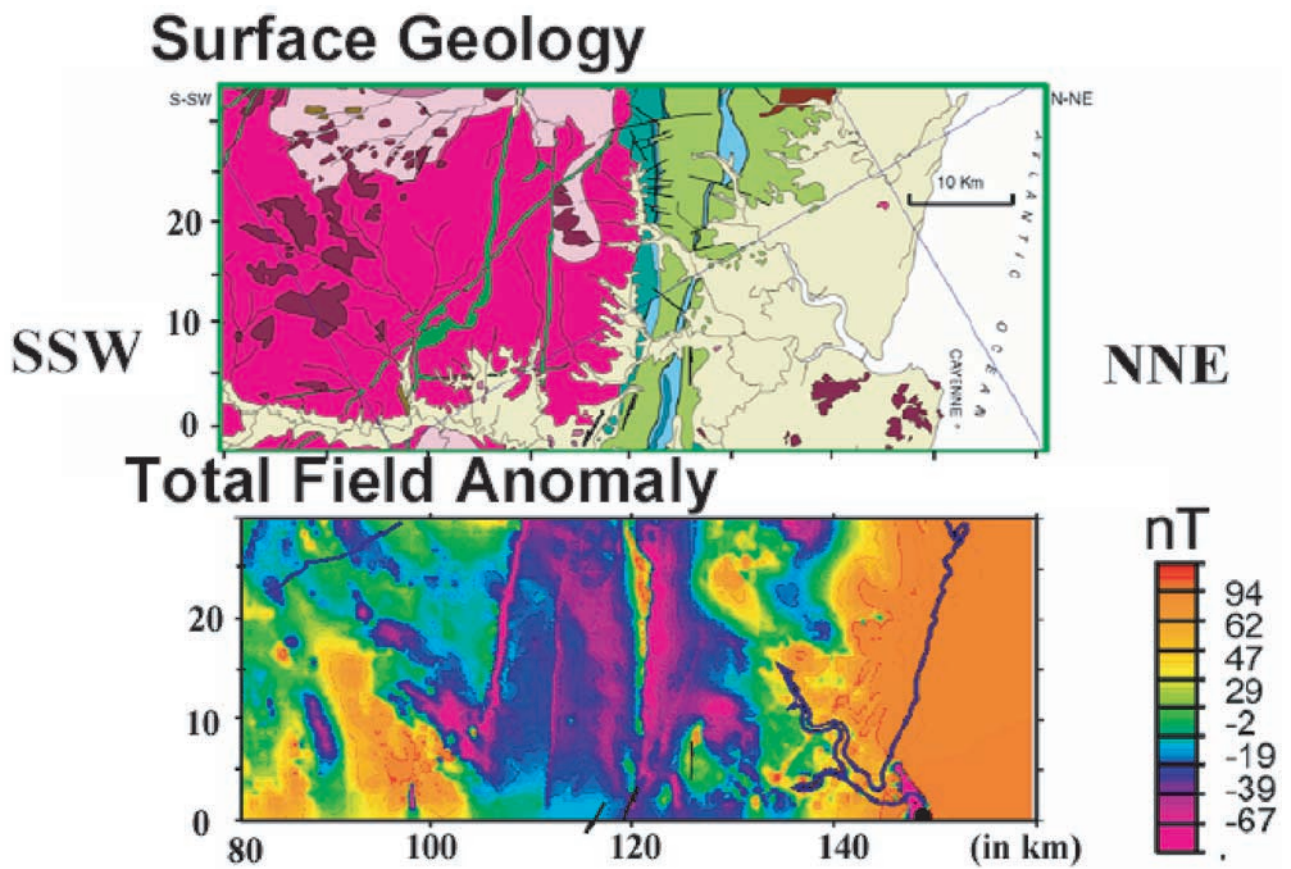


Figure 8. Data in French Guyana: Geological sketch and aeromagnetic map in SSW-NNE direction (see *Sailhac et al.* [2000] for geologic formations and reference coordinates).

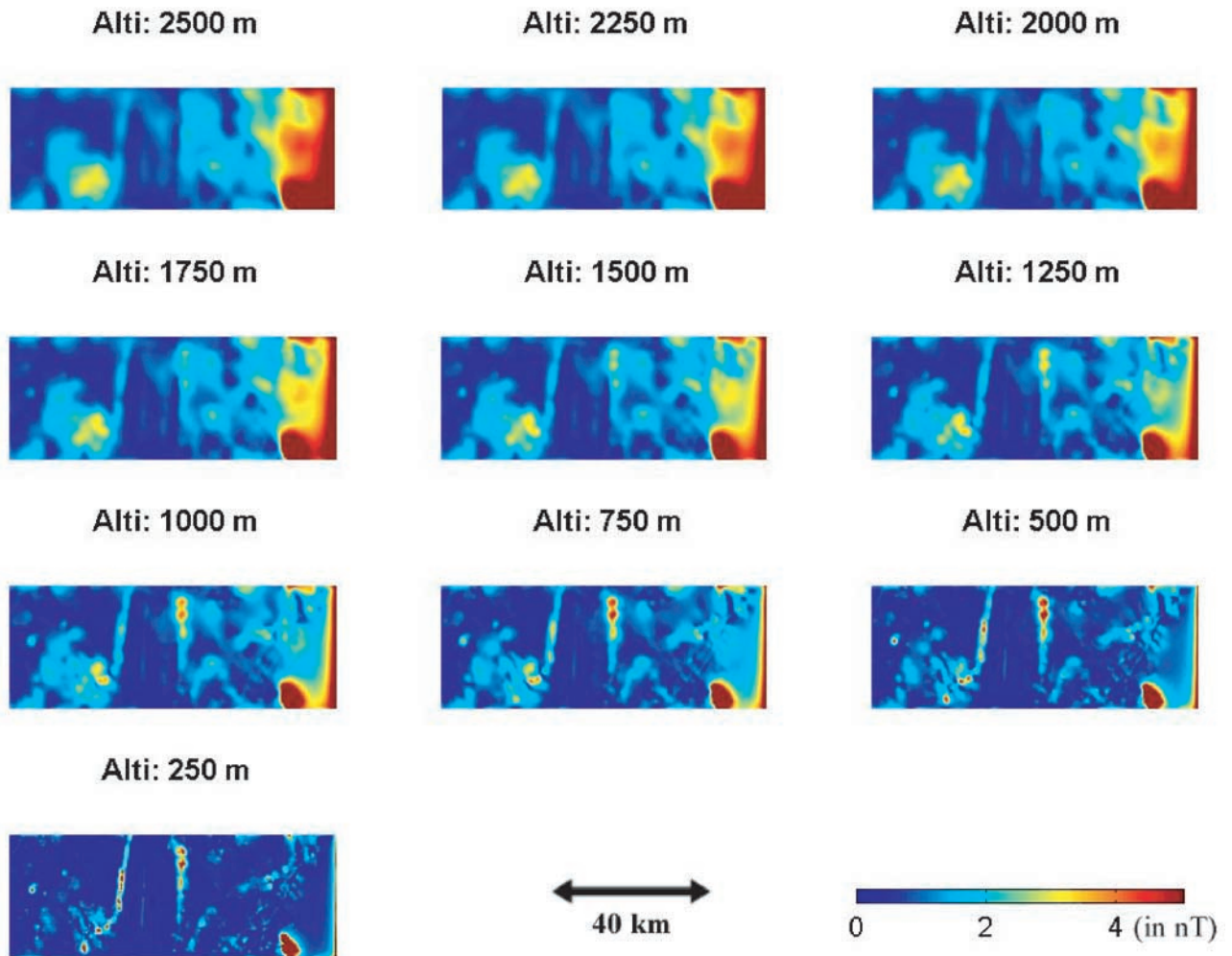


Figure 9. Wavelet transform of aeromagnetic map in Figure 8. Analytic wavelet coefficients (in nT) at various altitudes from 250 m up to 2500 km (each map is 80 km SSW by 30 km NNE).

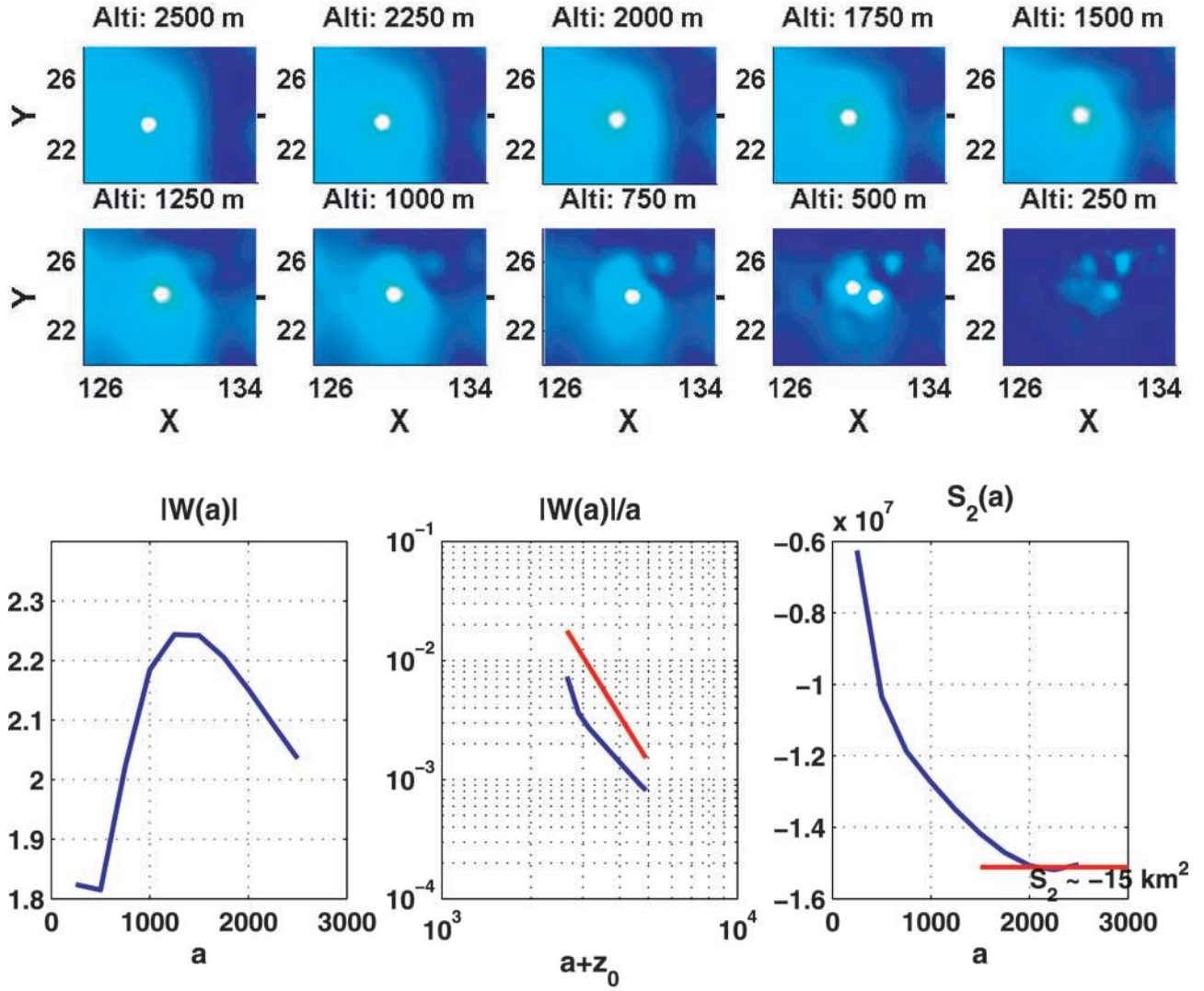


Figure 10. Interpretation of the wavelet transform modulus maxima of the aeromagnetic map in Figure 8. (top) Zoom (with same color scale as in Figure 9) of an area of $10 \text{ km} \times 8 \text{ km}$ where modulus maxima concentrate (white dots). (bottom) Interpretation functions based upon scaling of modulus maxima $|W|$: the log-log curve of $|W/a|$ for the depth estimation and the square function S_2 for the sizes.